Geophysical Journal International

Geophys. J. Int. (2022) **229,** 328–344
Advance Access publication 2021 November 26
GJI Geodynamics and Tectonics

https://doi.org/10.1093/gji/ggab477

Application of the mixing length theory to assess the generation of melt in internally heated systems

K. Vilella[1,2] and S. Kamata[2]

[1]*JSPS International Research Fellow, Hokkaido University, Hokkaido* 060-0808*, Japan. E-mail: kennyvilella@gmail.com*
[2]*Department of Earth and Planetary Sciences, Faculty of Science, Hokkaido University, Hokkaido* 060-0808*, Japan*

Accepted 2021 November 21. Received 2021 November 20; in original form 2021 June 2

SUMMARY

Melting in planetary mantles plays a key role in their thermochemical evolution. Assessing the amount and location of melting generally requires the 3-D temperature fields of the system, such that 3-D numerical simulations are in principle necessary prohibiting us from exploring wide ranges of conditions. To overcome this issue, we propose a new 1-D analytical framework estimating at first order the amount and depths of melting for a simplified convective system. To do so, we develop an approach, partly based on an extended version of the mixing length theory, able to estimate the distribution of the hottest temperatures in natural systems. The approach involves several free parameters that are calibrated by fitting 3-D numerical simulations. We demonstrate that our algorithm produces melting profiles at steady-state and long-term evolutions in fairly good agreement with 3-D numerical simulations. We then apply our framework to a wide variety of planetary sizes and heating rates. We find that an increase in planetary radius R increases the depth of melting for small planets ($R < 800$ km) but decreases it for larger planets. This is caused by the pressure dependence of the solidus.

Key words: Numerical modelling; Planetary interiors; Dynamics: convection currents, and mantle plumes; Heat generation and transport; Planetary volcanism.

1 INTRODUCTION

The thermochemical evolution of a planetary body is fundamental to determine its past and current state. For a terrestrial planet, this evolution is characterized by the coupling of different processes occurring in different parts of the planet and at different temporal and spatial scales. A usual way to circumvent the difficulty of modelling such a complex system is to focus on the long-term evolution of the planetary mantle. Indeed, because of its much slower dynamics compared to the atmosphere or the liquid iron core, the evolution of the mantle is believed to control the heat transfer of the planet's interior. However, modelling the dynamics of planetary mantles is in itself a complex problem.

One major issue is to account for the melting of rocks and the subsequent chemical differentiation and volcanism. Although 3-D numerical simulations consider increasingly sophisticated modelling of melting (Christensen & Hofmann 1994; Samuel & Farnetani 2003; Xie & Tackley 2004; Lourenço *et al.* 2018), the composition of the produced melt is generally prescribed and is independent of the depth and temperature of the molten rocks. While this simplification is required to reduce the computational time, it induces bias in the estimated long-term evolution, especially the location, quantity and composition of melt.

Alternatively, one may also use analytical models to account for the effects of melting on planetary evolutions (Breuer & Spohn 2003; Morschhauser *et al.* 2011; Grott *et al.* 2011). These previous works generally rely on a parametrized approach where scaling relationships are used to reconstruct an approximate average temperature profile. However, melting should not be estimated from the average temperature profile, but from the full lateral distribution of temperature. As a matter of fact, the average temperature can be significantly lower than the solidus, while locally the temperature is high enough to generate melt. Considering the average temperature profile to assess the generation of melting leads to a much lower volume of melt generated at greater depths (see for instance temperature profiles reported in Labrosse 2002).

In this work, we derive a new 1-D analytical framework to estimate at first order the amount and depths of melting. As 1-D models are not appropriate for estimating the full lateral distribution of temperature, we develop instead an approach, partly based on an extended version of the mixing length theory (MLT), able to estimate the cumulative distribution function of the hottest temperatures. In other words, our aim is not to constrain the precise lateral distribution of temperature but only the distribution of the hottest temperatures from a statistic/probability point of view. Due to the novelty of our approach, we apply our framework to a simplified convective system consisting of a purely internally heated fluid in a Cartesian geometry. This approach involves several free parameters that are calibrated by fitting 3-D numerical simulations (obtained previously in Limare *et al.* 2015; Vilella *et al.* 2018).

We then verify the accuracy of our analytical approach against 3-D numerical simulations. In that aim, we develop an algorithm calculating the evolution of a system experiencing secular cooling and melting. At last, this algorithm is used to investigate the influence of different parameters on the amount and depths of melting.

2 THEORETICAL CONSIDERATIONS

Before developing our extended version of the MLT, we give a short description of the convective system considered and a brief overview of the classical MLT. These preliminary considerations are crucial to understand the limitations and strengths of our theoretical approach.

2.1 Description of purely internally heated convection

As a reference set-up for our approach, we consider a purely internally heated fluid. This convective system generally consists in a horizontal layer of fluid, with a constant temperature imposed at the top boundary and an adiabatic condition at the base. Because of the adiabatic condition at the bottom, the only source of heat is volumetric heating, that is each parcel of fluid is homogeneously heated, and the heat escapes from the top boundary. When the fluid is further considered to be isoviscous and incompressible, the system is only controlled by the Rayleigh–Roberts number (Roberts 1967),

$$Ra_H = \frac{\rho g \alpha \Delta T_H d^3}{\kappa \eta}, \tag{1}$$

where

$$\Delta T_H = \frac{H d^2}{\lambda} \tag{2}$$

is the temperature scale of the system, ρ density, g the acceleration of gravity, α the thermal expansion coefficient, H the volumetric heating rate, d the layer's height, λ the thermal conductivity, κ the thermal diffusivity, and η viscosity. The Rayleigh–Roberts number quantifies the vigour of convection. With increasing Ra_H, the convective system becomes more and more chaotic, velocities increase and the lengthscale of convective structure decreases. As this convective system has already been extensively investigated (Parmentier & Sotin 2000; Vilella & Kaminski 2017), we will only mention few of its important characteristics. Note that, here and hereafter, we will use for illustration purposes the 3-D numerical simulations published in Vilella *et al.* (2018), obtained with StagYY (Tackley 2008) and described in Supplementary Text 1.

A brief look at the convective system (Fig. 1) indicates the presence of a top thermal boundary layer (TBL), where large vertical temperature variations occur, above an almost isothermal convective interior. The top TBL controls the dynamics of the system by generating cold downwellings that sink into the convective interior. As a result, a non-buoyant return flow is present in the convective interior to balance the input of sinking materials. However, a part of the cold material accumulates at the base of the system (Fig. 1b) inducing a slight decrease of the temperature with depth (Fig. 1a). This feature is called subadiabaticity and has been observed in various internally heated systems (e.g. Jeanloz & Morris 1987; Sinha & Butler 2007).

2.2 Fundamentals of the MLT

The MLT has been widely used to study turbulent convective systems, for example stellar convection (Vitense 1953; Spiegel 1963) or magma ocean solidification (Sasaki & Nakazawa 1986; Abe 1993). By contrast, applications to laminar convective systems are less common and mainly concern icy satellites (Kimura *et al.* 2009; Kamata 2018) or rocky planets (Tachinami *et al.* 2011; Wagner *et al.* 2019). Overall, the MLT is considered to be more accurate for complex convective systems than traditional approaches such as parametrized convection (Sharpe & Peltier 1978; Jellinek & Jackson 2015) or boundary-layer theory (Stevenson *et al.* 1983; Driscoll & Bercovici 2014). It is however important to keep in mind that the calibration of the MLT is becoming increasingly difficult as the system complexity increases.

The main purpose of the MLT is to estimate the 1-D thermal state of a system. To do so, the starting point is to consider the conservation of energy, which at steady state can be written as

$$0 = -\frac{\mathrm{d}F_{\mathrm{cond}}}{\mathrm{d}z} - \frac{\mathrm{d}F_{\mathrm{conv}}}{\mathrm{d}z} + H, \tag{3}$$

where z is height, $F_{\mathrm{cond}} = -\lambda \mathrm{d}T/\mathrm{d}z$ the conductive heat flux and F_{conv} the advective heat flux. Assuming H as independent from z, an integration of eq. (3) gives simply,

$$C = -F_{\mathrm{cond}} - F_{\mathrm{conv}} + Hz, \tag{4}$$

with C a constant to be determined. At the base of the system ($z = 0$), $F_{\mathrm{cond}} = 0$ and $F_{\mathrm{conv}} = 0$, because the base is adiabatic, implying $C = 0$. As a consequence, estimating the thermal state of the system consists in the determination of the advective heat flux F_{conv}. The specificity of the MLT is to obtain an approximate expression of this advective heat flux by neglecting the horizontal advection of heat, so that F_{conv} simply represents the vertical advection of heat. In that purpose, using the definition of the specific heat capacity $C_p = \lambda/\kappa\rho$, one can write that at first order

$$F_{\mathrm{conv}} = \overline{\rho C_p w \theta}, \tag{5}$$

where w is the vertical velocity and θ the temperature perturbation compared to the laterally averaged value. Note that here and hereafter the overbar denotes laterally averaged properties. Assuming a Stokes velocity for w, determining F_{conv} boils down to the determination of an appropriate expression for θ. To do so, the MLT focuses on a column of fluid and considers that the perturbation of temperature θ is caused by a fluid parcel transported from a height $z = z_0$ that was originally at ambient temperature $\overline{T(z_0)}$. This implies

$$T(z) = \overline{T(z_0)} + \frac{\mathrm{d}T}{\mathrm{d}z}(z - z_0). \tag{6}$$

Furthermore, by a lateral average of this equation we obtain

$$\overline{T(z)} = \overline{T(z_0)} + \frac{\mathrm{d}\overline{T}}{\mathrm{d}z}(z - z_0), \tag{7}$$

and when combining these two equations,

$$\theta = T(z) - \overline{T(z)} = \left(\frac{\mathrm{d}T}{\mathrm{d}z} - \frac{\mathrm{d}\overline{T}}{\mathrm{d}z}\right)(z - z_0). \tag{8}$$

We further note $l(z) = 2(z - z_0)$ the mixing length, that is corresponding to the typical length-scale where temperature perturbations are homogenized. Finally, following Sasaki & Nakazawa (1986), we incorporate the Stokes velocity

$$w = \frac{2l^2 g \alpha \rho \theta}{9\eta} \tag{9}$$

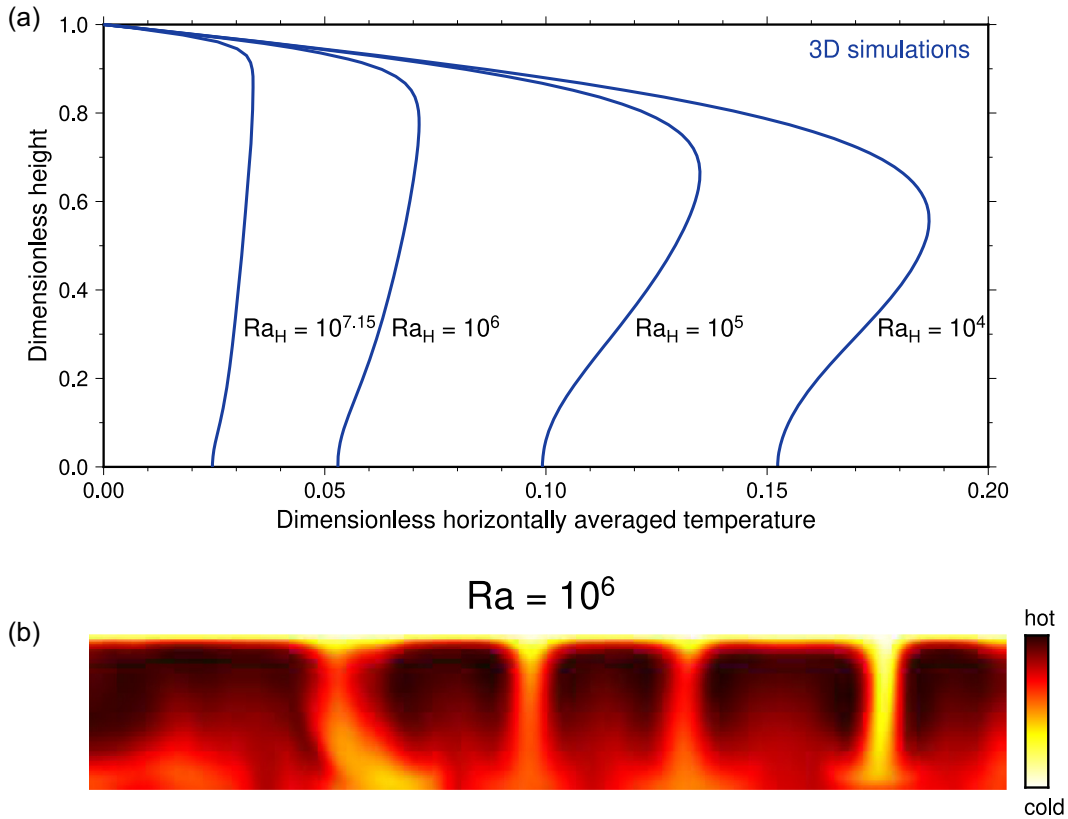

Figure 1. (a) Horizontally averaged temperature profiles obtained for various values of the Rayleigh–Roberts number (Ra_H). (b) Vertical slice of the temperature field obtained for $Ra_H = 10^6$. The results of (a) and (b) are from 3-D numerical simulations (see Vilella *et al.* 2018, for more details on the simulations).

and eq. (8) into eq. (5) to obtain

$$F_{\text{conv}} = \frac{\rho^2 C_p \alpha g l^4}{18\eta}\left(\frac{\mathrm{d}T}{\mathrm{d}z} - \frac{\mathrm{d}\overline{T}}{\mathrm{d}z}\right)^2. \tag{10}$$

Incorporating eq. (10) into eq. (4) and normalizing the equation with the temperature scale (eq. 2) and the layer's height d, we finally obtain

$$\frac{\mathrm{d}T^*}{\mathrm{d}z^*} - \frac{Ra_H l^{*4}}{18}\left(\frac{\mathrm{d}T^*}{\mathrm{d}z^*} - \frac{\mathrm{d}\overline{T^*}}{\mathrm{d}z^*}\right)^2 + z^* = 0, \tag{11}$$

where dimensionless values are denoted with a *. Eq. (11) is the main equation solved in the following section.

3 EXTENDED VERSION OF THE MLT

Our goal is to build an analytical framework able to estimate at first order the amount and depths of melting. Estimating the location and amount of melting requires to compare the solidus/liquidus profile with the distribution of temperature. Here, we focus on systems with a moderate amount of melting, so that only the distribution of the hottest temperatures is required. Furthermore, because the melting temperature of silicates is increasing with pressure/depth (e.g. Zhang & Herzberg 1994), the shape of the temperature profiles in Fig. 1(a) implies that melting should be mainly generated within the top TBL. Therefore, our main objective is to reproduce accurately the distribution of the hottest temperatures in the top TBL.

This process will be carried out in several stages. First, we propose a modification of the MLT providing a satisfactory estimate of the horizontally averaged temperature profile for purely internally heated fluids. We then apply this framework to determine the 'hot' temperature profile, that is composed of the hottest temperature at every depth. Finally, using the estimated hot and average temperature profiles, we develop a process to reconstruct the cumulative distribution function for the 5 per cent hottest temperatures.

3.1 Determination of the average temperature profile T^*_{avg}

The determination of the temperature profile using eq. (11) requires to prescribe a profile for l^* and $\mathrm{d}\overline{T^*}/\mathrm{d}z^*$. While l^* is generally assumed to be the closest distance from a horizontal boundary, the average temperature profile is difficult to evaluate *a priori*. As such, the MLT is generally used to study turbulent convection, since the average temperature is simply the adiabatic temperature profile. Following Kamata (2018), the adiabatic profile can also be used as a proxy for the average temperature profile in laminar convection. Provided that a modified expression for l^* is considered (Fig. 2), this approach is able to reproduce reasonably well numerical results (Kamata 2018; Wagner *et al.* 2019).

As a first step, we apply this formalism to internally heated convection. In that case, the adiabatic temperature profile is constant with depth so eq. (11) simply writes

$$\frac{\mathrm{d}T^*}{\mathrm{d}z^*} - \frac{Ra_H l^{*4}}{18}\left(\frac{\mathrm{d}T^*}{\mathrm{d}z^*}\right)^2 + z^* = 0. \tag{12}$$

This equation does not have a solution for $\mathrm{d}T^*/\mathrm{d}z^* = 0$ and $z^* > 0$ indicating that the temperature will continuously increase or decrease with depth. In practice, because the average temperature profile is maximum at the base of the TBL (Fig. 1), only the upper part of the TBL can be reproduced correctly. This formalism is

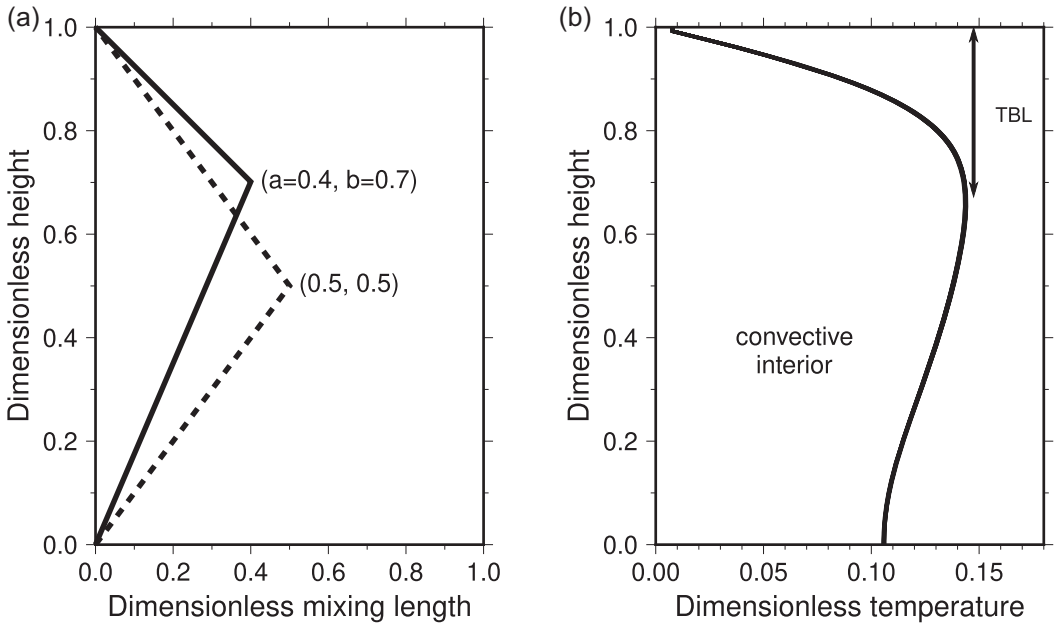

Figure 2. (a) Plots of the dimensionless mixing length (l^*) and (b) horizontally averaged temperature profile as a function of the dimensionless height. For the sake of simplicity, we characterize l^* with (a,b) where $l^*(b) = a$ is the maximum value of l^*. The dashed line represents the traditional mixing length (0.5, 0.5), while the solid line is an example of mixing length used here. Note that in our framework a is given by eq. (13) while $b = 1 - \delta^*_{\mathrm{TBL}}$ with δ^*_{TBL} the dimensionless thickness of the thermal boundary layer.

therefore not appropriate for the specific case of purely internally heated systems.

Alternatively, we propose to approximate $\mathrm{d}\overline{T^*}/\mathrm{d}z^*$ using a simple but unknown function (f^*) of z. By doing this, we depart from the framework used to establish eq. (11), but this approximation has the advantage of giving solutions for purely internally heated fluids. For the specific case $\mathrm{d}T^*/\mathrm{d}z^* = 0$, obtained at $z^* = 1 - \delta^*_{\mathrm{TBL}}$, eq. (11) implies

$$l^*(z = 1 - \delta^*_{\mathrm{TBL}}) = \left(\frac{18(1 - \delta^*_{\mathrm{TBL}})}{Ra_H f^*(z = 1 - \delta^*_{\mathrm{TBL}})^2} \right)^{1/4}, \tag{13}$$

with δ^*_{TBL} the thickness of the TBL. We can further assume that the mixing length is maximum at $z^* = 1 - \delta^*_{\mathrm{TBL}}$ (Fig. 2). In that case, solving eq. (11) only requires to know the value of f^* and δ^*_{TBL}. The latter can be obtained from numerical simulations, while the former has to be determined. Therefore, the main difficulty of our approach lies in the determination of a robust and convenient expression for f^*.

There are several possible methods to achieve this task. For instance, one may conduct a systematic search using a large range of functions to find one providing a good fit for the whole temperature profile. The risk of this method is to require a modelling of f^* so complex that it decreases the applicability of our approach. We therefore choose to put our emphasis on finding a simple expression, that is without an excessive number of parameters, that provides an accurate description of the TBL. As such, we simply consider

$$f^*(z^*) = c/z^{*d}, \tag{14}$$

where c and d are constants. In the original MLT, the function f^* is the gradient of the average temperature profile $\mathrm{d}\overline{T^*}/\mathrm{d}z^*$. Surprisingly, f^* is very different from $\mathrm{d}\overline{T^*}/\mathrm{d}z^*$ (Fig. S4), especially at $z^* = 0$ where f^* is divergent while $\mathrm{d}\overline{T^*}/\mathrm{d}z^*$ is equal to zero. Note however that the reason for this discrepancy can be explained by using scaling arguments (see Supplementary Text 2).

The next step is to calibrate the model parameters. To do so, we calculate the average temperature profile by solving eq. (11) (method described in the Appendix) for a large range of parameter values (c, d and δ^*_{TBL}). Then, for each Ra_H investigated, we identify the set of parameter values that minimizes the misfit between the analytical and numerical results. The objective of this is to establish scaling relationships characterizing the three parameters of the model. Interestingly, our results indicate that it seems reasonable to consider a constant value for c and d implying a function f^* that does not change with Ra_H (values reported in Table 1). δ^*_{TBL} is thus the only parameter function of Ra_H. Previous works on similar convective systems (e.g. Sotin & Labrosse 1999; Vilella & Kaminski 2017) have shown that it is possible to establish a scaling relationship for δ^*_{TBL} using a power-law function. Nevertheless, it is difficult to establish a single scaling relationship valid for the whole range of Ra_H because of the change in the convective structure, for example from time-independent structure at $Ra_H < 10^5$ to time-dependent structure at $Ra_H > 10^5$. Based on numerical results from Vilella & Kaminski (2017), it seems more appropriate to separate the range of Ra_H into three domains ($Ra_H < 10^5$, $10^5 \leq Ra_H < 10^7$ and $Ra_H \geq 10^7$), and, for each domain, conduct a best-fitting procedure using a power-law function. The results of the best-fit procedure are reported in Table 1. Using these relationships, we reconstruct the average temperature profile for each of our 3-D numerical simulations and plot some representative results in Fig. 3. To quantify the ability of our analytical method to reproduce numerical results, we calculate the coefficient of determination R^2 for each case and find an average value of 0.658. This low value is not surprising considering the significant temperature deviation occurring in the convective interior. However, this deviation is not necessarily an issue for our purpose as the melt generation is expected to occur in the top TBL where temperature variations are well reproduced ($R^2 = 0.998$).

The modified version of the MLT proposed in this section is therefore able to reproduce reasonably well the results of 3-D

Table 1. Parameters of the modified mixing length theory (see text for more details).

	Average temperature profile (T_{avg})
MLT (eq. 20)	$\frac{\mathrm{d}T^*_{\mathrm{avg}}}{\mathrm{d}z^*} - \frac{Ra_H l^*(z^*)^4}{18}\left(\frac{\mathrm{d}T^*_{\mathrm{avg}}}{\mathrm{d}z^*} - f^*(z^*)\right)^2 + z^* = 0$
Input function (eq. 14)	$f^*(z^*) = \frac{c}{z^{*d}}$ with $c = 0.05$ and $d = 1.55$
Mixing length (eq. 13)	$l^*(z = 1 - \delta^*_{\mathrm{TBL}}) = \left(\frac{18(1-\delta^*_{\mathrm{TBL}})}{Ra_H f^*(z = 1-\delta^*_{\mathrm{TBL}})^2}\right)^{1/4}$
	$Ra_H < 10^5$ $\quad 10^5 \leq Ra_H < 10^7$ $\quad 10^7 \leq Ra_H$
δ^*_{TBL}	$0.8241\,Ra_H^{-0.06637}$ $\quad 4.4412\,Ra_H^{-0.2203}$ $\quad 5.6885\,Ra_H^{-0.2352}$
	Hot temperature profile (T_{hot})
MLT (eq. 19)	$\frac{\mathrm{d}T^*_{\mathrm{hot}}}{\mathrm{d}z^*} - \frac{Ra_H l^*(z^*)^4}{18}\left(\frac{\mathrm{d}T^*_{\mathrm{hot}}}{\mathrm{d}z^*} - f^*(z^*)\right)^2 + Nu_{\max} z^* = 0$ with $Nu_{\max} = 1.65$ (Fig. S1)
Input function (eq. 14)	$f^*(z^*) = \frac{c}{z^{*d}}$ with $c = 0.055$ and $d = 1.52$
Mixing length (eq. 16)	$l^*(z = 1 - \delta^*_{\mathrm{TBL}}) = \left(\frac{18\,Nu_{\max}(1-\delta^*_{\mathrm{TBL}})}{Ra_H f^*(z = 1-\delta^*_{\mathrm{TBL}})^2}\right)^{1/4}$
	$Ra_H < 10^5$ $\quad 10^5 \leq Ra_H < 10^7$ $\quad 10^7 \leq Ra_H$
δ^*_{TBL}	$1.7881\,Ra_H^{-0.1558}$ $\quad 4.3793\,Ra_H^{-0.234}$ $\quad 4.6238\,Ra_H^{-0.2361}$
	Temperature distribution (g_{dist})
Eq. (18)	$T^*_{95} = n_{95}\,T^*_{\mathrm{avg}} + (1 - n_{95})\,T^*_{\mathrm{hot}}$ with $n_{95} = 1/3$
Cdf of the temperature between 95 and 100 per cent following eq. (17)	$g_{\mathrm{dist}} = 95 + 5\left[1 - \exp\left(-p\frac{T^* - T^*_{95}}{T^*_{\mathrm{hot}} - T^*_{95}}\right)\right]$ with $p = 5$

numerical simulations, and this for all values of Ra_H between 10^4 and 10^9. The next step of our study is to apply this framework to the hot temperature profile.

3.2 Determination of the hot temperature profile T^*_{hot}

The hot temperature profile is essentially similar to the horizontally averaged temperature profile, with the exception of the surface heat flux. Indeed, the average surface heat flux is, by construction, equal to Hd, while the surface heat flux calculated from the hot temperature profile is *a priori* unknown. Nevertheless, in our numerical simulations, its value only slightly varies between $1.52Hd$ and $1.75Hd$ (Fig. S1). We therefore decide to assume an intermediate value of $1.65Hd$ and modify accordingly eq. (11),

$$\frac{\mathrm{d}T^*}{\mathrm{d}z^*} - \frac{Ra_H l^*(z^*)^4}{18}\left(\frac{\mathrm{d}T^*}{\mathrm{d}z^*} - f^*(z^*)\right)^2 + 1.65z^* = 0, \tag{15}$$

and eq. (13),

$$l^*(z = 1 - \delta^*_{\mathrm{TBL}}) = \left(\frac{29.7(1-\delta^*_{\mathrm{TBL}})}{Ra_H f^*(z = 1-\delta^*_{\mathrm{TBL}})^2}\right)^{1/4}. \tag{16}$$

We can now estimate the model parameters (c, d and δ^*_{TBL}) for the hot temperature profile adopting the same procedure as in Section 3.1. The scaling relationship for each parameter is again reported in Table 1, while some representative results are shown in Fig. 4. Compared to the average temperature profile (Fig. 3), the fit of the TBL is slightly less satisfying ($R^2 = 0.998$ and 0.993, respectively), especially for low values of Ra_H. By contrast, because the subadiabacity is less pronounced, the convective interior is better fitted ($R^2 = 0.866$ compared to $R^2 = 0.658$ for the average temperature profile). Overall, the calculated hot temperature profiles are in good agreement with 3-D numerical results.

3.3 Determination of the temperature distribution

The last step is to estimate the distribution of the hottest temperatures using both the average and hot temperature profiles obtained above. Here, we will mainly focus on the distribution of temperature at a given depth using the cumulative density function (cdf). A brief explanation of the cdf is provided in Fig. 5. Although the precise shape of the distribution changes with Ra_H (Vilella *et al.* 2018), the main characteristics remain similar independently of the Ra_H and depth considered. First, the cumulative density function slowly increases until values up to 0.1–0.2, then sharply increases until reaching 0.95–0.98, and again slowly increases until 1.0. The fitting of this type of distribution is challenging. In particular, the extreme values of the distribution will often be grossly misfitted by classical distribution functions, while being crucial for our purpose.

To overcome these difficulties, we only focus on the hottest temperatures, here taken as the cdf between 0.95 and 1. Interestingly, when these distributions are rescaled, that is the dimensions of both the x-axis and y-axis are modified in order to range from 0 to 1 (Fig. 6), they exhibit a similar trend, independently of the depth or Ra_H. We can therefore estimate this part of the distribution using a simple function. For instance,

$$g^*_{\mathrm{dist}} = 1 - \exp(-pT^*_{rsc}), \tag{17}$$

with p a fitting parameter and T^*_{rsc} the dimensionless and rescaled temperature, provides a good fit (Fig. 6). The best-fitting value of the parameter p changes with the depth and Ra_H considered and ranges typically between 1 and 10. Here, for the sake of simplicity,

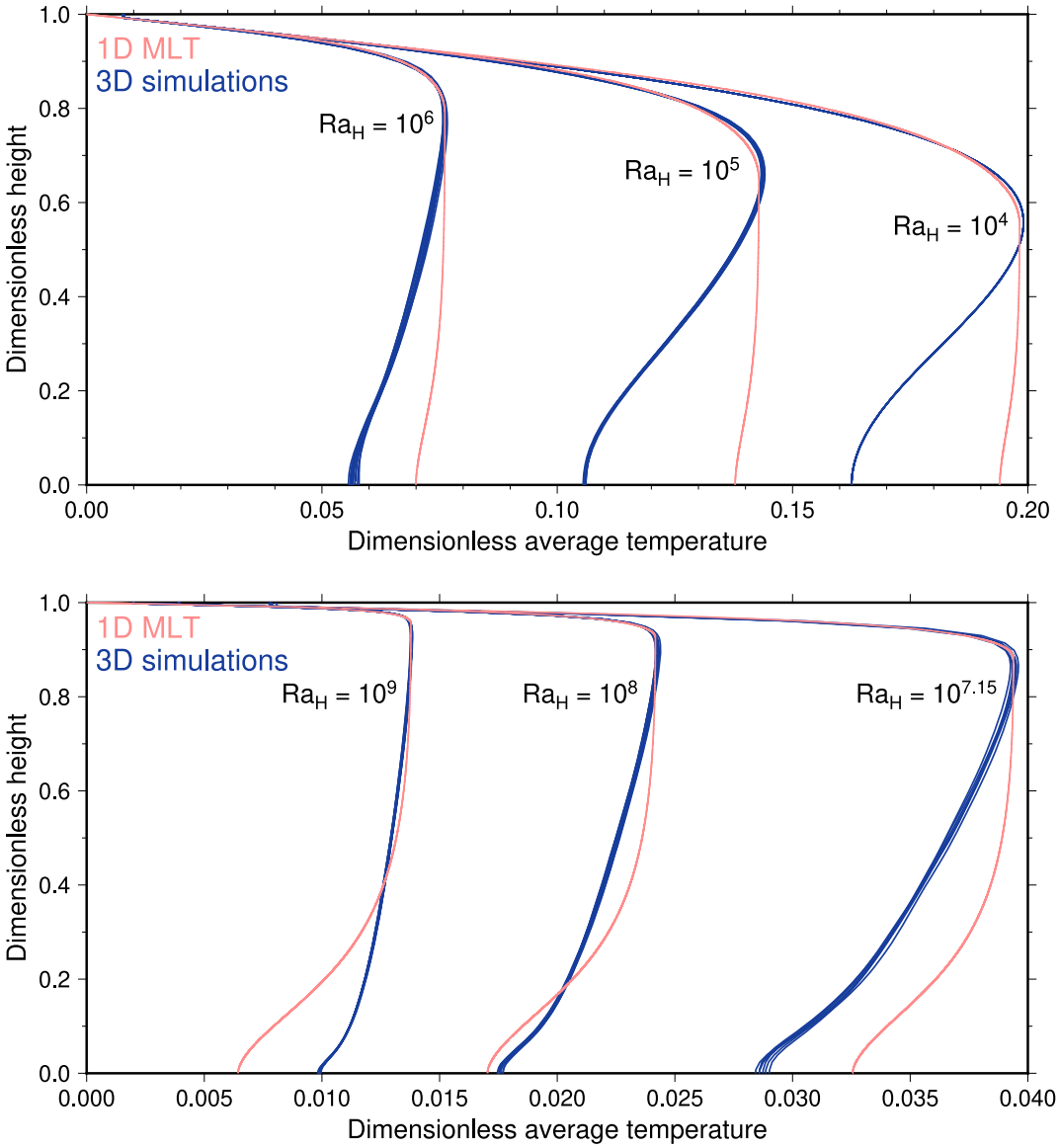

Figure 3. Horizontally averaged temperature profiles from 3-D numerical simulations and calculated using the mixing length theory for various values of the Rayleigh–Roberts number (Ra_H). Profiles at different time-steps are reported to account for temporal variations.

we consider a constant value $p = 5$ as it provides a distribution in fairly good agreement with numerical results (Fig. 6).

To obtain the original distribution of temperature from the rescaled one, it is necessary to estimate the temperature profile corresponding to a cdf of 95 per cent (T^*_{95}). Based on empirical observations, we calculate this profile assuming, at first order, that

$$T^*_{95} = (1/3)\, T^*_{\mathrm{avg}} + (2/3)\, T^*_{\mathrm{hot}}. \tag{18}$$

Our analytical results are plotted in Fig. 7 along with results from 3-D numerical simulations. For $Ra_H < 10^7$, the profiles agree reasonably well in the TBL with only slight differences that are equivalent to the ones found for the average (Fig. 3) and hot (Fig. 4) temperature profiles. For $Ra_H > 10^7$, the agreement is less satisfactory, with a slight overestimation of the temperatures at the base of the TBL. Nevertheless, close to the base of the TBL (where the differences are larger), the disagreement is lower than 5 per cent for all the cases studied. Results given by eq. (18) are therefore accurate enough for our purpose.

3.4 Summary of the key stages of our method

At that point, we have all the necessary ingredients to estimate, at given conditions, the distribution of the 5 per cent hottest temperatures and thus to estimate the generation of melt in a natural system. For the sake of clarity, we provide in this section a brief summary of this process. The first step is to build the dimensionless hot (T^*_{hot}) and horizontally averaged (T^*_{avg}) profile using

$$\frac{\mathrm{d}T^*_{\mathrm{hot}}}{\mathrm{d}z^*} - \frac{Ra_H l^{*4}}{18}\left(\frac{\mathrm{d}T^*_{\mathrm{hot}}}{\mathrm{d}z^*} - \frac{0.055}{z^{*\,1.52}}\right)^2 + 1.65z^* = 0 \tag{19}$$

and

$$\frac{\mathrm{d}T^*_{\mathrm{avg}}}{\mathrm{d}z^*} - \frac{Ra_H l^{*4}}{18}\left(\frac{\mathrm{d}T^*_{\mathrm{avg}}}{\mathrm{d}z^*} - \frac{0.05}{z^{*\,1.55}}\right)^2 + z^* = 0, \tag{20}$$

respectively. In these equations, the profile of the mixing length l^* is indicated in Fig. 2, while its maximum value is given by eqs (16) and (13), respectively. Note that the parameter values are reported in Table 1. The second step is to use eq. (18) to calculate T^*_{95}, the

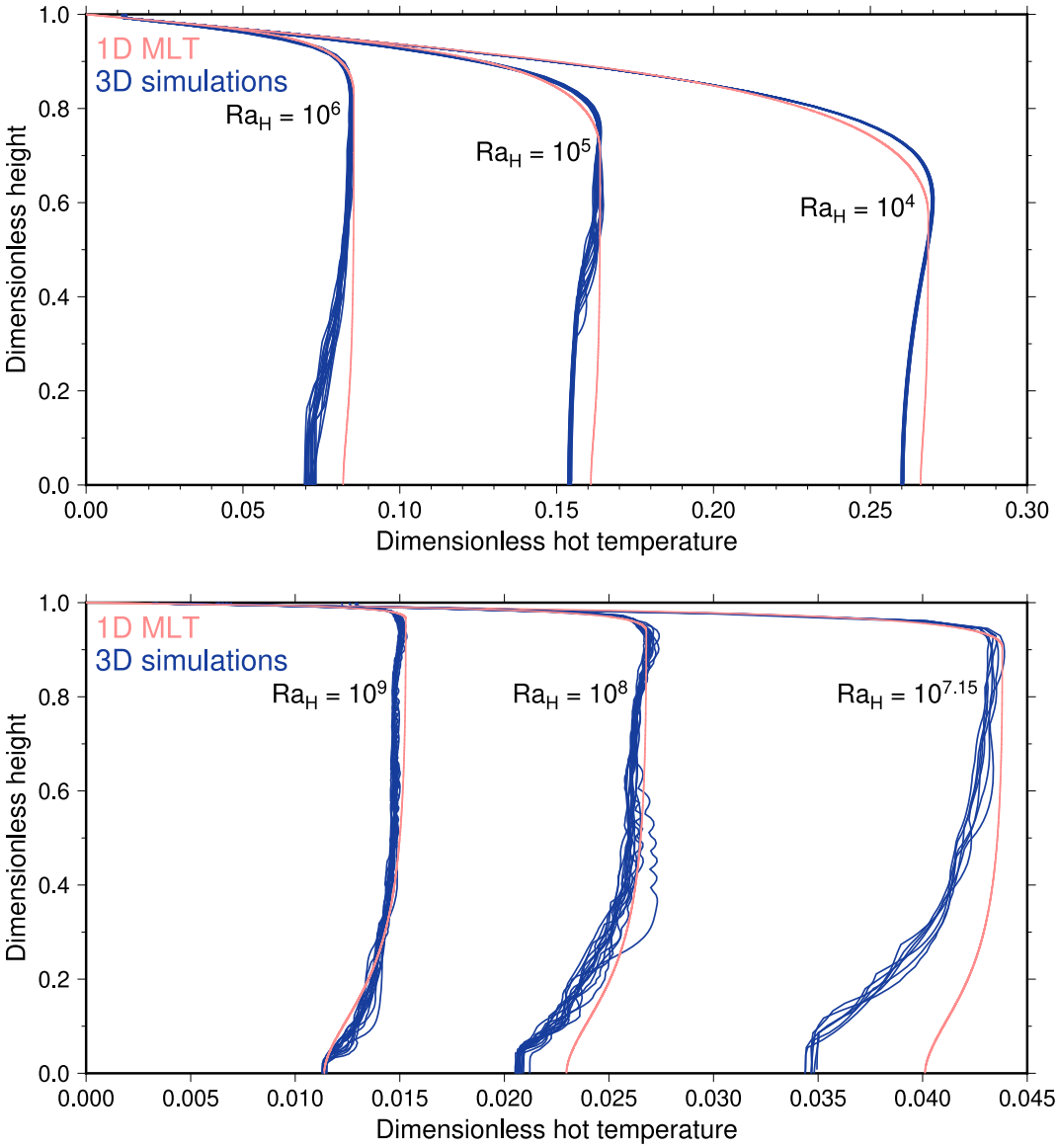

Figure 4. Hot temperature profiles from 3-D numerical simulations and calculated using the mixing length theory for various values of the Rayleigh–Roberts number (Ra_H). Profiles at different time-steps are reported to account for temporal variations.

temperature profile corresponding to a cumulative density function of 95 per cent. It is then possible to calculate at every depth the distribution of temperature between T^*_{95} and T^*_{hot} using eq. (17), with $p = 5$. The last step is to dimensionalize the calculated distribution of temperature using the temperature scale of the system (eq. 2). These distributions can then be used to estimate the generation of melt in a natural system. However, our approach relies on a large number of assumptions, each one having intrinsic uncertainties. It is therefore important to test the accuracy of our method in practical cases.

4 PRECISION OF THE ANALYTICAL APPROACH

The aim of this section is to estimate the potential accuracy of our analytical approach when applied to a natural system. A direct application may however be misleading, since our model assumes a too simple set-up to be applied to an actual planetary body, for instance, viscosity variations and compressibility effects are neglected. We therefore chose to apply our analytical approach to a generic planetary mantle. This gives a first indication on the performance of our analytical model, which is crucial before attempting to extend the approach to actual systems. The evaluation will be conducted in two stages. First, we will compare 1-D analytical results and 3-D numerical results at steady state for various Ra_H in the range 10^4–10^9 in order to confirm that, at first order, the 1-D analytical results are consistent with results of 3-D simulations. Then, we will use a more sophisticated model to estimate the evolution of a generic planetary mantle using both our analytical approach and the numerical code StagYY (Tackley 2008).

4.1 Silicate mantle at steady state

The first test will be conducted as follows: (i) we will calculate the analytical results corresponding to each of our 3-D numerical simulations; (ii) the analytical and numerical results will be applied

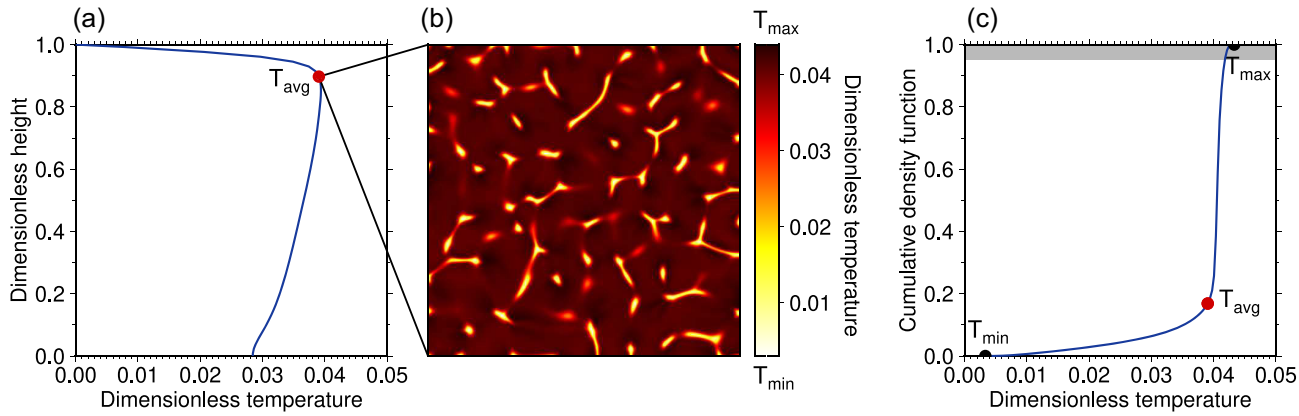

Figure 5. Illustration of the cumulative density function (cdf) using the 3-D numerical simulation obtained for $Ra_H = 10^{7.15}$. At a given depth, here taken as a dimensionless height equal to 0.9, that is the base of the thermal boundary layer in (a) the average temperature profile, (b) the temperature field exhibit large lateral variations. These variations can be quantified using the (c) cdf. The cdf measures the proportion of material with a temperature lower than the temperature considered. For instance, a cdf of 0.5 indicates the median temperature, while a cdf of 0 and 1 indicate that there is no temperature lower or higher, respectively, than the temperature considered. The average (T_{avg}), minimum (T_{min}) and maximum (T_{max}) temperature at that depth are indicated in (c), while the shaded area corresponds to the distribution of temperature between a cdf of 0.95 and 1.0 reported in Fig. 6.

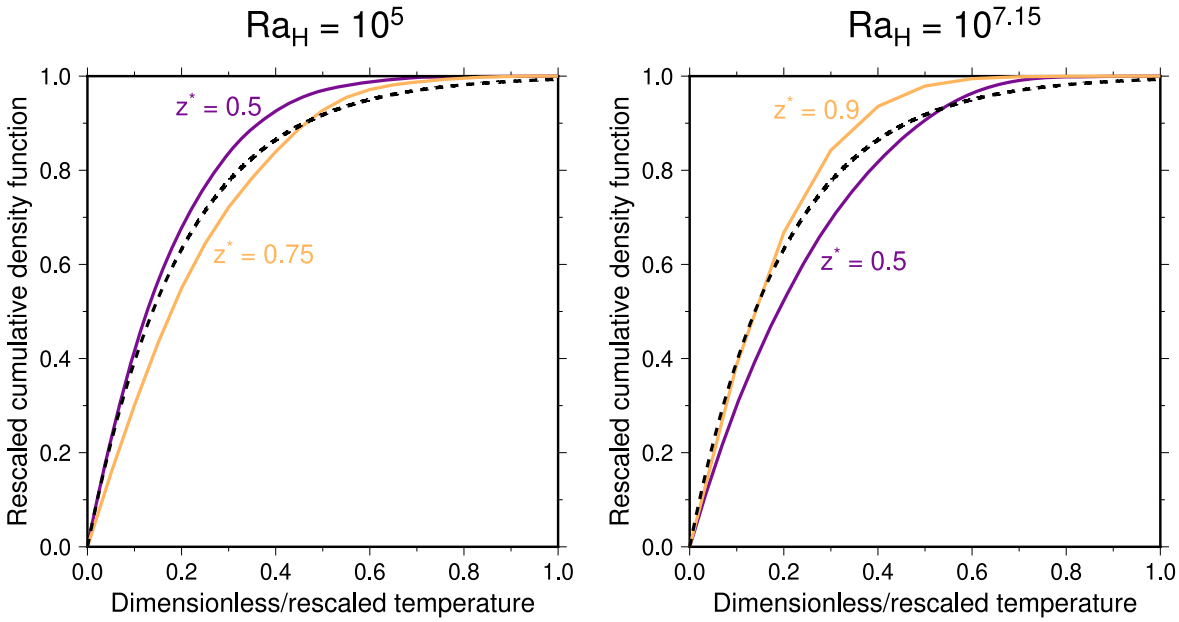

Figure 6. Distributions of temperature from 3-D numerical simulations taken at different depths for $Ra_H = 10^5$ (left-hand panel) and $Ra_H = 10^{7.15}$ (right-hand panel). The plots focus on the 5 per cent hottest temperatures, where melting is potentially occurring. When the distributions are rescaled, they show a similar behaviour that can be fitted with eq. (17) (dashed line), here showed for $p = 5$.

to a generic mantle. In particular, we will estimate the proportion of material above the melting temperature as a function of depth and (iii) we will compare the two sets of results to evaluate the accuracy of our analytical approach. Using the line of reasoning developed in Section 3, the calculation of the analytical results is straightforward. It only requires to dimensionalize the results and set the solidus profile.

The temperature scale of the system is given in eq. (2) and depends on the heating rate (H_{tp}), the mantle depth (d_{tp}) and its thermal conductivity (λ_{tp}). For the sake of example, we decide to study a 1000 km deep generic planetary mantle composed of silicates. Under this assumption, typical values for the properties of silicates are reported in Table 2 along with other important properties. Note that different values could have been considered without affecting our conclusions. The last parameter needed to calculate the temperature scale is H_{tp}. We investigate a large range of values for H_{tp}, but only focus on cases with a moderate amount of melt. The quantity of melt generated is estimated by comparing the calculated temperatures to a solidus profile (Fig. S2) obtained from an interpolation of experimental works on terrestrial peridodites (Zhang & Herzberg 1994; Hirschmann 2000; Andrault *et al.* 2011), while the pressure is assumed to be hydrostatic. As such, we do not estimate the amount of melt generated, but the proportion X_M of material with a temperature larger than the solidus profile. Note that the amount of melt generated will be investigated in the next section.

The analysis of our results has shown that all the cases investigated could be separated into two groups depending on their Ra_H. We therefore report in Fig. 8 only one representative case for each group. For cases with $Ra_H \leq 10^7$ (Fig. 8a), the predicted temperature profiles are in relatively good agreement with profiles obtained

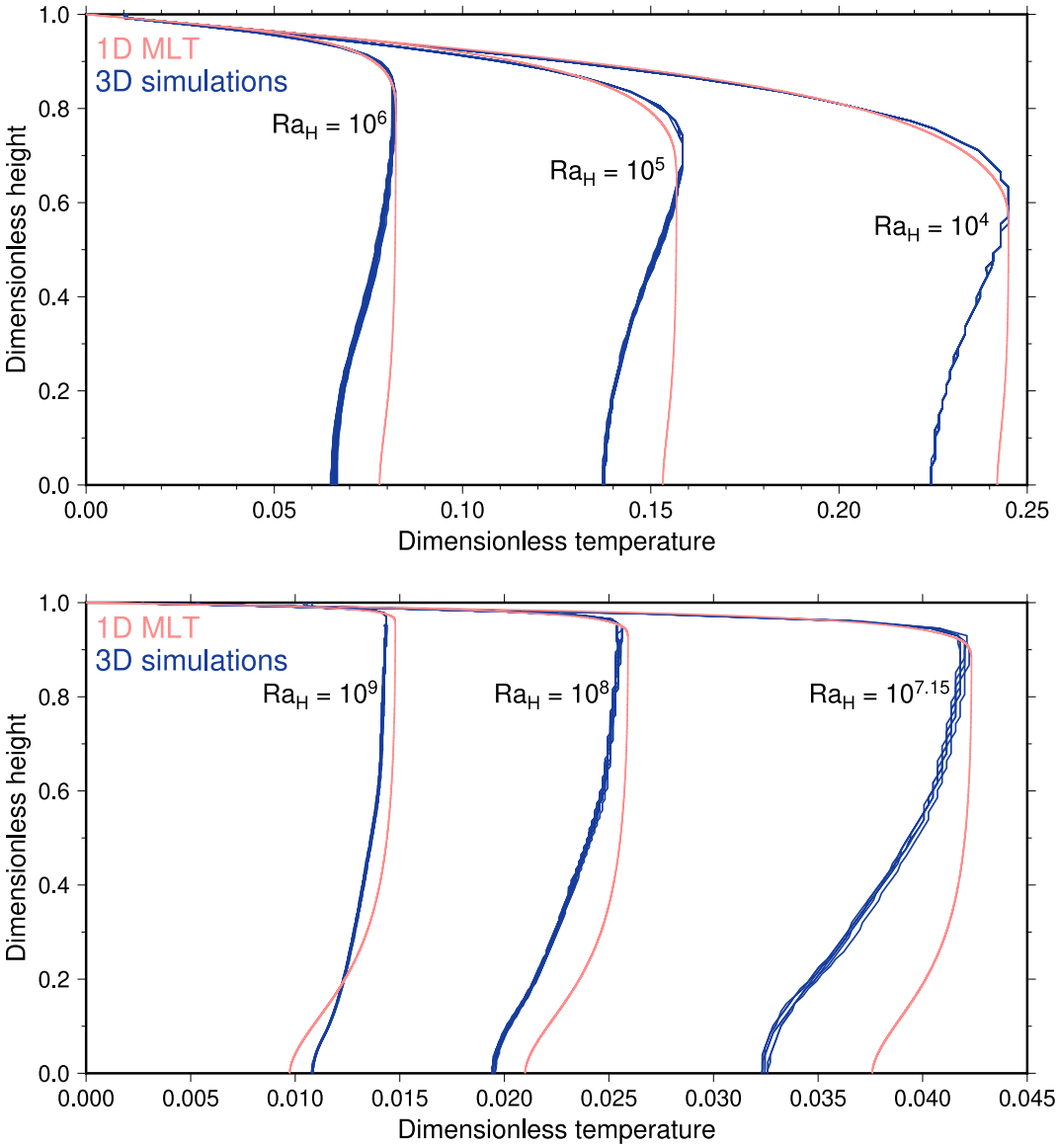

Figure 7. Temperature profiles corresponding to a cumulative density function of 95 per cent from 3-D numerical simulations and calculated by our approach for various values of the Rayleigh–Roberts number (Ra_H). Profiles at different time-steps are reported to account for temporal variations. The analytical curves are calculated using eq. (18) and the profiles predicted in Figs 3 and 4.

Table 2. Model parameters for our generic planetary mantle.

Parameter	Symbol	Value	Unit
Mantle depth	d_{tp}	1000	km
Gravity acceleration	g_{tp}	3.0	m s^{-2}
Surface temperature	$T_{\mathrm{surf},\,tp}$	250	K
Density	ρ_{tp}	3400	kg m^{-3}
Thermal conductivity	λ_{tp}	3.0	W m^{-1} K^{-1}
Thermal expansion coefficient	α_{tp}	5×10^{-5}	K^{-1}
Thermal diffusivity	κ_{tp}	7×10^{-7}	m^2 s^{-1}
Specific heat capacity	$C_{p,\,tp}$	1260	J kg^{-1} K^{-1}
Viscosity	η_{tp}	10^{20}	Pa s
Latent heat of fusion	L_{tp}	600	kJ kg^{-1}
Half-life ^{238}U	$t_{1/2}$	4.468	Gyr
Initial heating rate	H_{tp0}	2.45×10^{-7}	W m^{-3}

in numerical simulations ($R^2 > 0.99$ in the TBL, while $R^2 \approx 0.7$ for the whole profile), and the proportion of material with a temperature larger than the solidus profile agrees with the 3-D numerical results. To achieve this, however, we have considered a slightly different heating rate between the analytical and numerical results. If we assume the same value, Fig. S3 shows that the temperature profiles are visually identical, but the amplitude of X_M is systematically underestimated or overestimated. This is because the amplitude of X_M is very sensitive to variations of H_{tp} (e.g. Vilella *et al.* 2020). For all the numerical simulations investigated (i.e. even for lower Ra_H), the difference in H_{tp} required to obtain the same amplitude of X_M in the analytical and numerical results is lower than 4 per cent (an average of ≈2 per cent, which is consistent with typical errors of scaling laws). The effect of this difference on the amount of melt predicted is quantified in the next paragraph. For cases with $Ra_H \geq 10^7$ (Fig. 8b), the temperature profiles are also well reproduced by our analytical results ($R^2 > 0.99$ in the TBL, while $R^2 \approx 0.8$

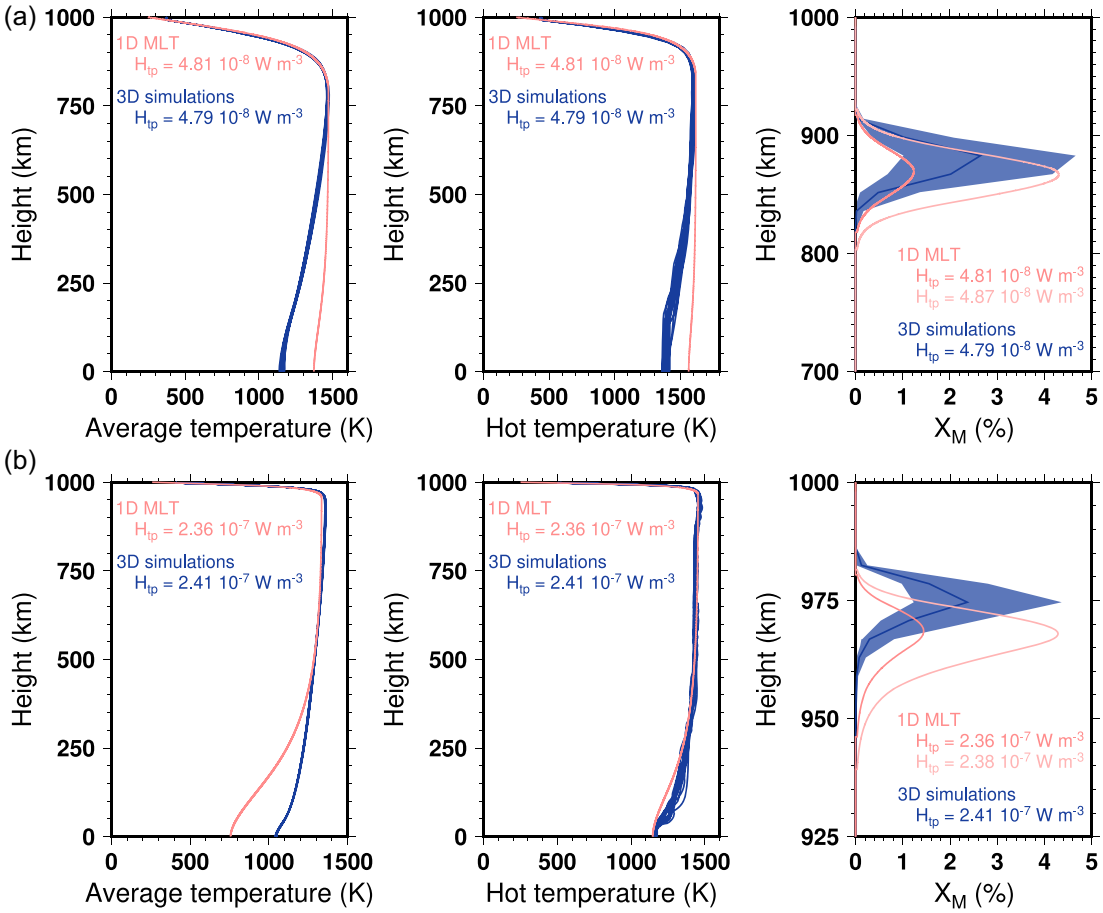

Figure 8. Horizontally averaged (left-hand column) and hot (central column) temperature profiles as well as X_M the proportion of material whose temperature is larger than the solidus temperature (right-hand column) for (a) $Ra_H = 10^6$ and (b) $Ra_H = 10^9$. Note that a different vertical scale is used in the right column for visualization purposes. Results obtained from both 3-D numerical simulations and our analytical framework are reported. In the right column, two different heating rates (H_{tp}) are considered in order to reproduce the temporal fluctuations exhibited by the 3-D numerical results (shaded area).

for the whole profile). Nevertheless, a slight disagreement exists between the two sets of results for X_M. Indeed, the maximum of X_M is slightly deeper in the analytical results (for $Ra_H = 10^9$, 32 km deep versus 25 km deep). This rather small difference (0.7 per cent of the mantle depth) is equivalent to the vertical resolution of our 3-D simulation (4 km resolution) and also equivalent to the typical errors expected from scaling laws of δ_{TBL} (Vilella & Kaminski 2017). We therefore conclude that, despite the simplifications, our analytical framework is able to provide a reasonable estimate of the location and proportion of material above the melting point.

4.2 Evolution of a generic planetary mantle

In the previous section, we have shown that our analytical approach should theoretically be able to estimate the melt generation for a wide range of Ra_H. We however used a simplified model assuming a steady-state without the effects of melting on the heat budget. These results may thus in practice not be applicable to the evolution of planets. Here, we therefore aim to verify the accuracy provided by our framework in the modelling of planetary evolution. This will be done in several steps. First, we develop an algorithm to estimate the evolution of a planetary mantle including the effects of melting and secular cooling. This model is then applied to the generic mantle described in the previous section. As a second step, we conduct a numerical simulation of this generic mantle using StagYY (Tackley 2008). Finally, we compare the results obtained with the two approaches.

4.2.1 Analytical estimation of the mantle evolution

The evolution of our generic mantle is mainly governed by its conservation of energy,

$$\rho_{tp} C_{p,tp} \frac{\mathrm{d}T}{\mathrm{d}t} = -\frac{\mathrm{d}F_{\mathrm{cond}}}{\mathrm{d}z} - \frac{\mathrm{d}F_{\mathrm{conv}}}{\mathrm{d}z} + H_{\mathrm{rad}} - \frac{P_{\mathrm{melt}}}{V}, \tag{21}$$

with H_{rad} the heating rate produced by radioactive heating, P_{melt} the power used for melting, V the volume of the mantle and t time. This equation is *a priori* different from the equation used in our analytical framework (eq. 3), so that a direct application may not be possible. However, if we simply write,

$$H_{\mathrm{melt}} = \frac{P_{\mathrm{melt}}}{V}, \quad H_{\mathrm{sec}} = \rho_{tp} C_{p,tp} \frac{\mathrm{d}T}{\mathrm{d}t}, \quad \text{and}$$
$$H_{\mathrm{eff}} = H_{\mathrm{rad}} - H_{\mathrm{melt}} - H_{\mathrm{sec}}, \tag{22}$$

then eq. (21) implies

$$0 = -\frac{\mathrm{d}F_{\mathrm{cond}}}{\mathrm{d}z} - \frac{\mathrm{d}F_{\mathrm{conv}}}{\mathrm{d}z} + H_{\mathrm{eff}}, \tag{23}$$

which is identical to eq. (3). It seems therefore possible to use our framework to estimate the distribution of temperature as long as H_{eff}

is assumed to be independent from z. Note that this is not entirely correct because both secular cooling and melting vary spatially. Nevertheless, the equivalence between secular cooling and a homogeneous heating source is often assumed (e.g. Krishnamurti 1968; Weinstein & Olson 1990; Davaille & Jaupart 1993) and has been confirmed empirically by Grasset & Parmentier (1998) in a system without melting. By contrast, the assumption that melting can be approximated by a homogeneous heating source has not yet been investigated. This is however out of the scope of this paper.

The effective heating rate $H_{\rm eff}$ is composed of three components (eq. 22). The first component, the radioactive heating contribution, is calculated using

$$H_{\rm rad} = H_{tp0} \exp\left(-\log(2)\frac{t}{t_{1/2}}\right), \tag{24}$$

with H_{tp0} the initial heating rate and $t_{1/2}$ the half-life of the radioactive isotopes. The main long-lived radioactive isotopes in terrestrial planets are ^{238}U, ^{235}U, ^{232}Th and ^{40}K. As the proportion of these radioactive isotopes may vary importantly depending on the planetary body considered, we follow a general approach by assuming only the presence of ^{238}U with an initial abundance set to obtain a moderate amount of melting. Note that when investigating a specific planet, one may easily incorporate additional radioactive isotopes. The second component corresponds to the power associated with melt generation,

$$H_{\rm melt} = \frac{L_{tp}\rho_{tp}\Delta V_{\rm melt}}{\Delta t\, V}, \tag{25}$$

with $\Delta V_{\rm melt}$ the volume of melt generated during the time-step of the evolution model Δt and L_{tp} the latent heat of fusion. Note that we here assume that all the material above the solidus is fully molten and instantaneously extracted to the surface (Section 5.1.5 provides a detailed discussion on this assumption). Therefore, the determination of $\Delta V_{\rm melt}$ only requires to compare the solidus profile with the estimated distribution of temperature. This assumption is made in order to increase the sensitivity of our analytical model to the input parameters. In other words, our goal is to estimate the maximum error between the numerical and analytical results. The third component corresponds to secular cooling. In practice, we calculate this contribution using,

$$H_{\rm sec} = \rho_{tp} C_{p,tp} \frac{\Delta T_{\rm vol}}{\Delta t}, \tag{26}$$

with $\Delta T_{\rm vol}$ the variation of the volume average temperature between the time t and $t + \Delta t$. Note that all the properties of the model are reported in Table 2.

Following eqs (25) and (26), the effective heating rate $H_{\rm eff}$ is a function of the thermal state of the mantle, while $H_{\rm eff}$ is required to estimate the distribution of temperature. One has therefore to follow an iterative process to obtain the actual thermal state (so $H_{\rm eff}$) of the system. In order to improve the speed and accuracy of our numerical scheme, we decided to calculate *a priori* the temperature and melting profiles for a large range of $H_{\rm eff}$. As a result, at each time-step, the actual $H_{\rm eff}$ can simply be obtained by solving eq. (23) using the pre-calculated data. Once the value of $H_{\rm eff}$ is obtained, we move to the time $t + \Delta t$ and repeat the process until the full evolution is calculated.

An interesting feature of this model is that the effective heating rate decreases, at first order, with Δt (eqs 25 and 26). It is therefore possible to lower the amount of melt produced by reducing the time-step used. This is a crucial feature because our framework is only able to predict, at a given depth, a maximum melt proportion of 5 per cent. Decreasing the time-step can therefore be used to overcome this limitation (see Section 5.1.5 for more details). However, a small time-step would induce a large computational time. We therefore use a small time-step in eq. (25), set by the need to have a low proportion of melting, while we use a time-step Δt_{ev} = 10 000 yr for the time-stepping procedure (and in eq. 25). This should have no impact on the results as long as the change of $H_{\rm eff}$ remains modest between t and $t + \Delta t_{\rm ev}$. In our case, this condition implies that $\Delta t_{\rm ev}$ has to be lower than 100 000 yr (Fig. S6).

4.2.2 *Numerical simulations of the mantle evolution*

The numerical simulation is designed to reproduce as closely as possible our analytical framework. As such, we consider a simplified version of melting, where all the volcanism is extrusive, all material above solidus is fully molten, and melt is instantaneously extracted to the surface. The rock properties are given in Table 2 and the heating rate is specified in eq. (24). The initial temperature condition is obtained by running a numerical simulation, with a constant heating rate H_{tp0}, until a steady-state is reached. This has the advantage to decrease the transient effects at the start of the simulation (see Section 5.1.3 for more details). The grid resolution and aspect ratio are 512 × 256 × 256 and 4:2, respectively. Grid refinement is used at the surface to improve the resolution of the TBL.

4.2.3 *Comparison between 1-D analytical evolution and 3-D simulation*

The comparison between the two approaches can be done using a variety of characteristics. Here, we have selected the following properties: (i) the maximum and volume average temperature in the mantle, to assess the thermal evolution and (ii) the depths where melting occurs and the rate of melt production $R_{\rm melt}$, to assess the melt generation. These properties are straightforward to obtain except the melting rate that is calculated at each time-step using

$$R_{\rm melt} = \frac{\rho_{tp} C_{p,tp}}{\Delta t\, V L_{tp}} \int_V (T - T_{\rm sol}) {\rm d}V, \tag{27}$$

with T the local temperature, and $T_{\rm sol}$ the local solidus temperature.

We report in Fig. 9 the evolution of the four selected properties for both the 1-D analytical model and the 3-D simulation. We first note that the evolution of the maximum temperature is fairly well reproduced by the analytical approach with a typical deviation lower than 50 K (≈6 per cent, Fig. 9a). By contrast, the volume average temperature is systematically underestimated by ∼50–80 K (≈6–10 per cent, Fig. 9b). The latter is however not surprising as our analytical approach tends to underestimate the temperature in the convective interior for very large Ra_H (Fig. 3; Section 3.1). A close inspection of these plots reveals two important shortcomings of our analytical approach: (i) the analytical approach predicts an almost constant temperature and melting depths for almost 1 Gyr, whereas it is continuously decreasing in the simulation. This difference may be due to the difficulty of accounting for the dynamic nature of a convective system in an analytical approach based on a sequence of static snapshots (see Section 5.1.5 for more details). (ii) even though we tried to reduce the transient effects, we can still observe a slight transient phase in the first 300 Myr. This transient phase is caused by the inadequacy between the initial condition and the equilibrium state of the system. As the system naturally tends to reach equilibrium, a gradual change of its thermal state occurs with an increase of the mean temperature and a decrease of the maximum temperature, which in turn induces a slight decrease of the melting rate (Figs 9a, b and d). Transient effects may be important for the

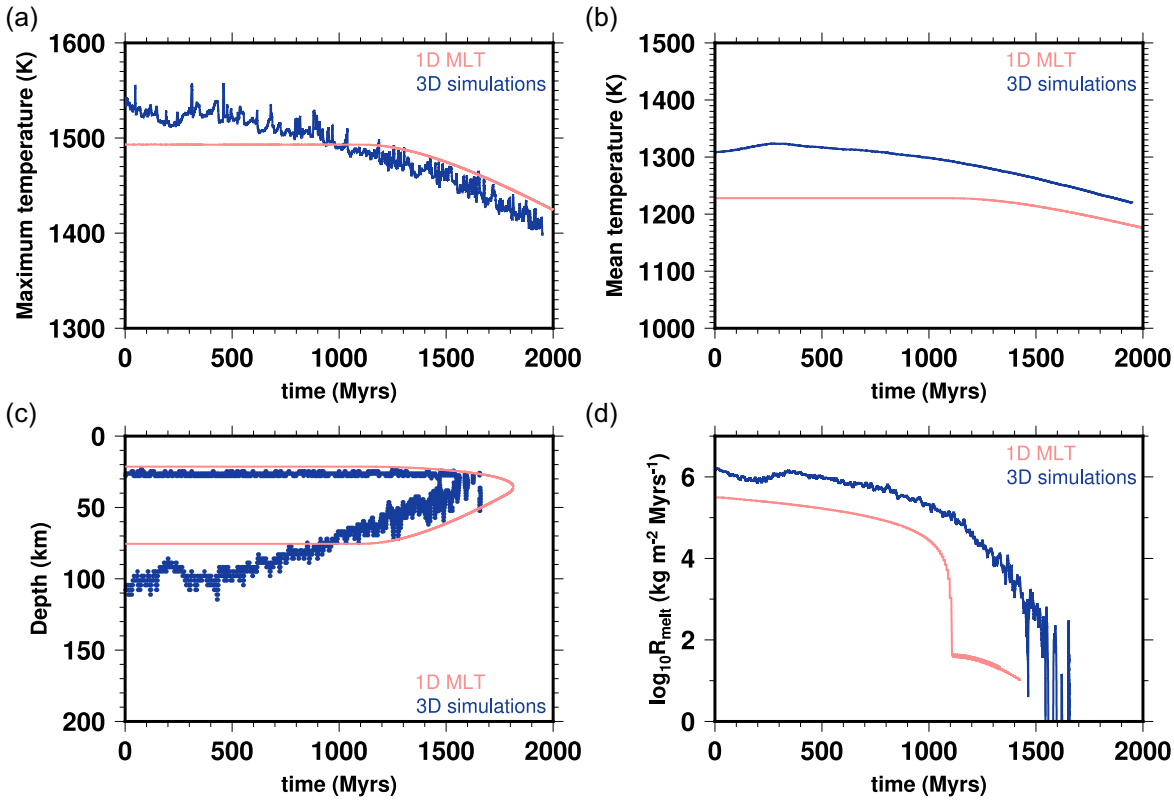

Figure 9. Evolution of the (a) maximum temperature, (b) the volume average temperature, (c) the depths where melting occurs and (d) the melting rate for the generic mantle described in Section 4.1. Results obtained from both 3-D numerical simulations and our analytical framework are reported.

early evolution of planetary bodies, while being difficult to account for in 1-D analytical models (see Section 5.1.3 for more details). With these two shortcomings in mind, we can now describe the evolution of the melt generation. In both the analytical approach and 3-D simulation, melting is present for an extended period of time and stops at ∼1.6 Gyr (Fig. 9c). The depths where melting occurs are well reproduced by the analytical approach, especially the initial depth range where melting occurs (∼60–100 km) and the decreased depth range with time. The only notable difference concerns the amplitude of the melting rate that is systematically underestimated by a factor 3 in the analytical calculation (Fig. 9d).

The comparison between the 1-D analytical evolution and 3-D simulation has shown that some properties, such as the maximum temperature or the depth range where melting occurs, are relatively well reproduced by our analytical approach, while other properties, such as the volume average temperature or melting rate, are subject to systematic deviations. By comparison, using the horizontally averaged temperature profile to assess the presence of melt, as done by previous studies (Morschhauser *et al.* 2011; Grott *et al.* 2011), leads to a period where melting occurs about 4.5 times shorter, while the power available for melting is about 30 times lower. In that sense, our method provides a net improvement in accuracy and stands therefore as a useful tool to study the evolution of planetary bodies.

5 DISCUSSION

5.1 Limitations

The approach developed in this study is subject to several important limitations. While some of these limitations can be easily alleviated, some others are inherent to the model and should be kept in mind. We provide in this section a brief discussion of these limitations.

5.1.1 Applicability domain

To start the discussion, it is important to mention that the laws built in this work are only valid for the specific conditions investigated. In particular, it would be hazardous to apply our results to systems with Ra_H much larger than 10^9. Indeed, the calculated temperature profiles are very sensitive to the value of δ_{TBL}. So the inevitable error on δ_{TBL} made when extrapolating the scaling laws may lead to large errors on the calculated temperature profiles. We would like to emphasize that this limitation is not specific to our work. Scaling laws are traditionally established by fitting numerical, experimental or empirical results with a power-law function (e.g. Silveston 1958; Castaing *et al.* 1989). This process is intrinsically flawed by the existing trade-off between the value of the pre-factor and the value of the exponent. While errors on the pre-factor are not dramatic, errors on the exponent would grow exponentially leading to large uncertainties when extrapolated over several orders of magnitude. As a general rule, scaling laws should therefore only be used to interpolate results.

5.1.2 Model complexity

This study considers a simplified convective system with only internal heating. Although this system is appropriate for some natural systems such as planetary bodies with large amount of tidal heating (e.g. for Io, Steinke *et al.* 2020) or radioactive heating (e.g. for the early evolution of planetesimals, Kaminski *et al.* 2020), its potential

applications are limited as several important ingredients are missing, for example basal heating or spherical geometry. Theoretically, the approach developed here can also be applied to more complex systems provided that a few modifications are adopted. First, the MLT eq. (11) should be adapted to the considered system. For instance, when both basal and internal heating are present, eq. (11) becomes

$$\frac{\mathrm{d}T^*}{\mathrm{d}z^*} - \frac{Ral^{*4}}{18}\left(\frac{\mathrm{d}T^*}{\mathrm{d}z^*} - \frac{\mathrm{d}\overline{T^*}}{\mathrm{d}z^*}\right)^2 + Nu_T - H(1-z^*) = 0, \quad (28)$$

where

$$Ra = \frac{\rho g \alpha \Delta T d^3}{\kappa \eta}, \quad (29)$$

is the Rayleigh number, ΔT the temperature jump across the system and Nu_T the dimensionless surface heat flux. Secondly, the shape of the mixing length (Fig. 2a) should also be adapted to the expected temperature profile. For instance, when basal heating is significant, a bottom TBL is present and the convective interior may be sub-adiabatic (i.e. with a negative temperature gradient). In that case, the mixing length should have a double peak, one for each TBL. After the implementation of these modifications, the last step is to determine scaling laws for the thickness of the two TBLs and for the function f^* (eq. 14). Note that the difficulty of this task increases with the complexity of the system.

5.1.3 Transient effects

Transient effects are particularly important in the early evolution of planets. Right after the planet formation, the whole planet, including the mantle, is unlikely to be at steady state, but rather in a much hotter state. The planetary mantle may even be fully molten and experience a magma ocean event (e.g. Monteux *et al.* 2016). As a consequence, the mantle evolution is characterized by a first phase, possibly lasting for several hundred million years, where it cools down until reaching a steady state. This first phase may be crucial in planetary evolution because it can potentially impact the whole subsequent evolution, as it has been postulated for instance for the Moon (Laneuville *et al.* 2013) or Earth (Ballmer *et al.* 2017). Generally, it is believed to be difficult to include these transient effects in 1-D analytical models. However, some previous works (Choblet & Sotin 2000; Limare *et al.* 2021) have suggested that scaling laws established at steady state remain valid in the transient phase allowing the introduction of transient effects in analytical models. Nevertheless, one may keep in mind that we have very few constraints on the early evolution of planets. Therefore, even if we could model accurately these transient effects, a lot of uncertainties would remain on the early evolution of planets because of our lack of constraints.

5.1.4 Secular cooling

Results of our 1-D analytical evolution show a systematic underestimation of the volume average temperature (∼70 K). Although it does not directly impact the generation of melting, it still influences the results as it may change the degree of secular cooling (eq. 26). In our case, the temporal derivative of the volume average temperature, which sets the amplitude of secular cooling, is similar in the 1-D analytical evolution and 3-D numerical simulation (Fig. 9b). Secular cooling should thus be correctly estimated. This may however not be always true. In particular, when the Rayleigh–Roberts number is changing by several orders of magnitude throughout the calculated evolution, one may expect a non-systematic error on the volume average temperature, which in turn may lead to a significant error on the amplitude of secular cooling. Nevertheless, for a typical terrestrial planet, large temporal variations of the Rayleigh–Roberts number are not expected so that our approach may be accurate. One should however remain careful when investigating evolutions exhibiting large temporal variations of the Rayleigh–Roberts number.

5.1.5 Melting process

Our model assumes a simple version of melting where at each time-step all the melt is reaching instantaneously the surface (extrusive volcanism). This assumption underlies several important simplifications. First, in a planetary setting, a non-negligible proportion of the melt would actually not reach the surface but would remain in the mantle and solidify (intrusive volcanism). The exact ratio between intrusive and extrusive volcanism is difficult to estimate, such that it is often considered as an input parameter in 3-D simulations. Secondly, melting ascent is not instantaneous, although it is much faster than the typical convective time-scale. Lastly, all material above the solidus is not fully molten but experiences partial melting producing chemical differentiation. One may note that these limitations are not peculiar to our analytical approach as they are also present in 3-D numerical simulations. Different methods developed to account for some of these complexities could be included in our model (e.g. Katz *et al.* 2003; Driscoll & Bercovici 2014). Here, the use of a simple version of melting was not dictated by an intrinsic limitation of our model, but because the aim of this study is only to show the validity of our approach and not to provide a realistic modelling of mantle evolution.

Our analytical approach has however an additional intrinsic limitation that induces a connection between time-step and melt generation. A simple way to identify this connection is by considering the extreme case of a very small time-step Δt. For such a case, following eqs (22) and (25), the volume of melt produced ΔV_{melt} has to be very low in order to maintain a reasonable value for the effective heating rate H_{eff}. In this extreme case, melt generation would only occur at a specific depth and at a specific temperature. This limitation comes from the dynamic nature of a convective system and can be understood by considering the evolution of hot upwellings. Generally, hot upwellings are rising through the convective interior due to their buoyancy. At one point, the plume head may cross the solidus and start to generate melt. The first generation of melt would however not stop the plume motion, such that the hot material would keep rising and producing melt over a certain depth range. Unfortunately, this dynamic process cannot be reproduced in an analytical approach relying on static snapshots of the convective system. Here, we thus tried to account for this limitation by setting a time-step value leading to a maximum proportion of material experiencing melting (P_{mm}) around 4.5 per cent. A different value of P_{mm} could be selected inducing changes in the calculated evolution.

In order to evaluate the consequences of this choice on our model results, we plotted in Fig. 10 the calculated evolutions assuming a value for P_{mm} of 4.5 per cent (as in Fig. 9), 2.0 and 0.5 per cent. As predicted, the depths where melting occurs is the most impacted property with a reduction of the depth range as P_{mm} decreases. Interestingly, this reduction is mainly caused by the decrease of the estimated maximum depth of melting for a low maximum proportion of melt (P_{mm} <2 per cent). By contrast, the estimated minimum depth of melting is only slightly affected indicating that it is a robust output of our model. We also note that the maximum temperature follows a similar behaviour than the maximum depth of melting,

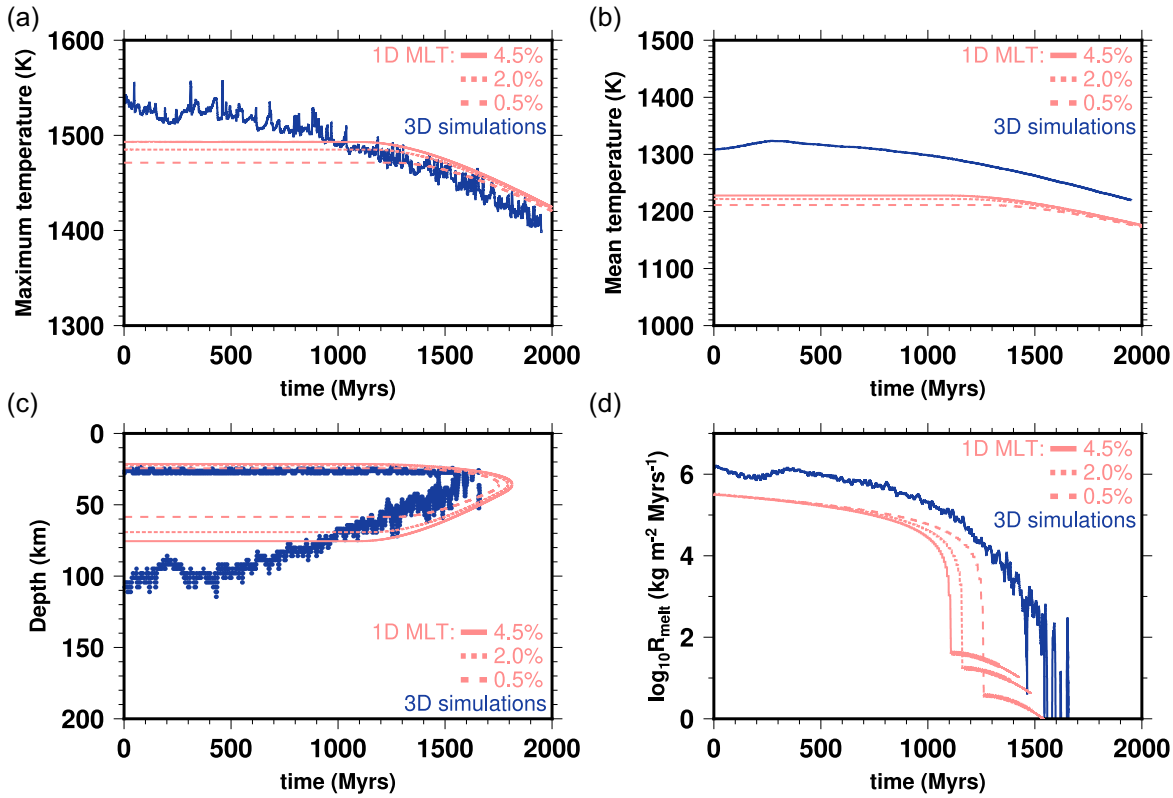

Figure 10. Evolution of the (a) maximum temperature, (b) the volume average temperature, (c) the depths where melting occurs and (d) the melting rate for the generic mantle described in Section 4.1. Solid curves are from Fig. 9, while dotted and dashed lines are obtained favouring a maximum amount of melting of 2.0 and 0.5 per cent, respectively.

while the volume of melt produced and its duration are hardly affected. For reference, the total volume of melt is ∼10 per cent lower when assumed $P_{\rm mm} = 4.5$ per cent compared to $P_{\rm mm} = 0.5$ per cent. Intuitively, the melting rate should not be impacted by our choice of $P_{\rm mm}$. However, increasing $P_{\rm mm}$ induces an increase in the average temperature of melt, so that more heat is required to produce the same amount of melt. As a result, the total volume of melt generated decreases with $P_{\rm mm}$, although the amount of heat available for melting is roughly similar. Note that it is not strictly similar because higher values of $P_{\rm mm}$ also implies a hotter initial temperature profile, so that more secular cooling is available (Fig. S5).

Overall, we conclude that only the maximum depth where melting occurs and the maximum temperature may be significantly affected by this limitation. For instance, this limitation is responsible for the constant maximum temperature and melting depths for the first 1 Gyr in Fig. 9. Nevertheless, our choice for $P_{\rm mm}$ (i.e. 4.5 per cent) seems to be high enough to provide a reasonable estimate for these properties, as shown by the results in Fig. 9. A higher value of $P_{\rm mm}$ (4.5–4.9 per cent) can also be considered as long as it remains lower than the maximum value accepted by our model (5 per cent). The reason is simply that our analytical method cannot estimate the melt volume for $P_{\rm mm} > 5$ per cent introducing a numerical singularity at $P_{\rm mm} = 5$ per cent. We therefore suggest to use $P_{\rm mm} = 4.5$–4.9 per cent for the analytical evolution while remaining cautious when analysing the maximum depth where melting occurs.

5.2 Implications for melting in exoplanets

A unique characteristic of our approach is to provide a fast first order estimate of the melt generation. This ability may be particularly useful when studying poorly constrained terrestrial planets, since a thorough numerical investigation would require a large calculation power. Here, we show an example of application by investigating the generation of melt in exoplanets.

Following the model used by Vilella & Kaminski (2017), we consider a differentiated terrestrial planet with a radius R_{tp} and a heating rate H_{tp}. The mass of the planet (M_{tp}) is obtained using the mass-radius relationship obtained by Valencia *et al.* (2006) for Earth-like planets,

$$\frac{R_{tp}}{R_T} = \left(\frac{M_{tp}}{M_T}\right)^{0.27}, \tag{30}$$

where R_T and M_T are the radius and mass of the Earth, respectively. We can then calculate the acceleration of gravity $g_{tp} = G\, M_{tp}/R_{tp}^2$, with G the gravitational constant. The mantle depth (d_{tp}) is estimated using (Valencia *et al.* 2006),

$$d_{tp} = R_{tp} - R_{c,tp} \quad \text{with} \quad R_{c,tp} = 3.5\,10^3 \left(\frac{R_{tp}}{R_T}\right)^{0.926}, \tag{31}$$

the core radius (all the distances are in kilometres). By contrast with Vilella & Kaminski (2017), we do not consider a temperature dependent viscosity nor the effects of spherical geometry. Furthermore, values for rock properties are listed in Table 2 and slightly differ from the ones used in Vilella & Kaminski (2017), in particular the pressure is here assumed to be hydrostatic.

Using this set of parameters combined with our analytical approach, we estimate the generation of melting for a large range of planetary radius and heating rates assuming a maximum amount of melt of 4.5 per cent (see Section 5.1.5). As a first step, we identify the conditions for which the Rayleigh–Roberts number is either too

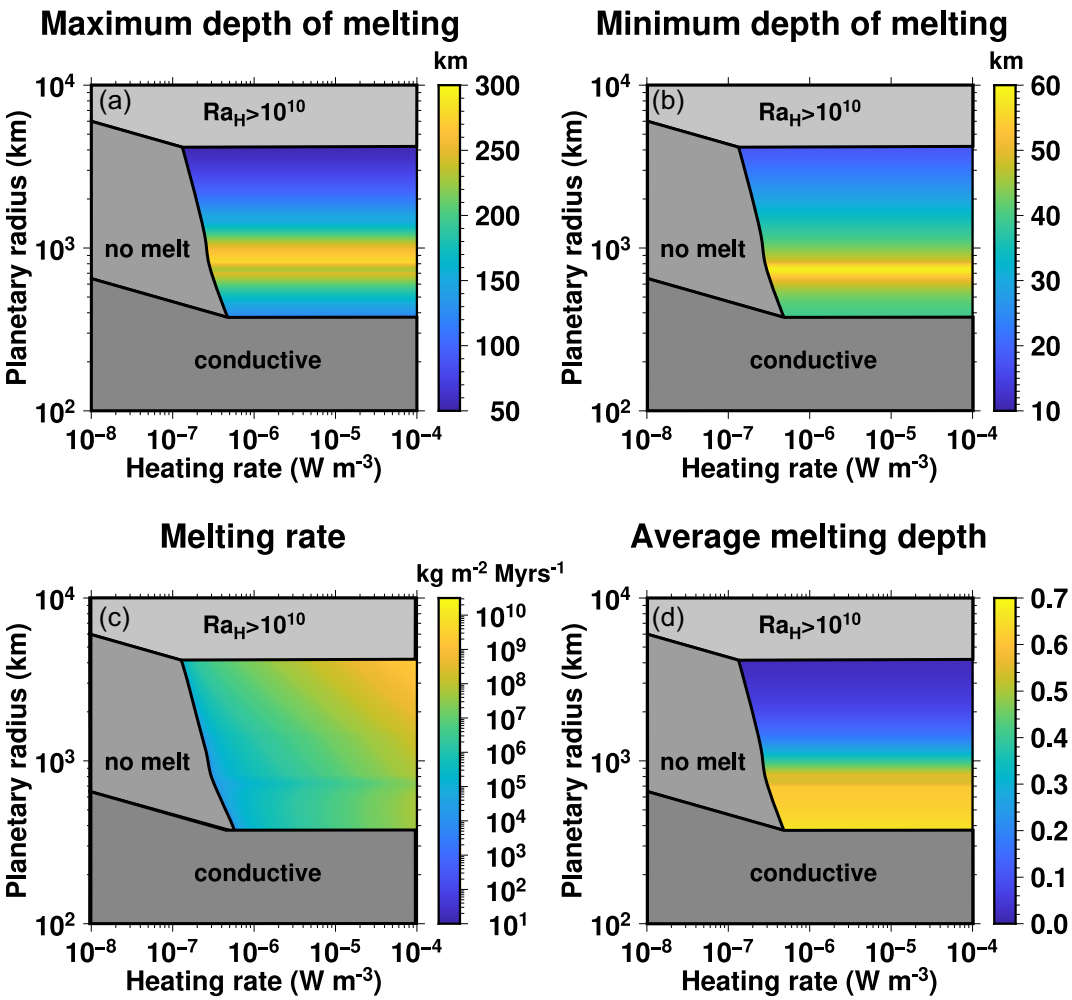

Figure 11. Diagram showing the estimated (a) maximum depth of melting, (b) minimum depth of melting, (c) melting rate and (d) dimensionless average melting depth as a function of the planetary radius and heating rate. We exclude the cases where the natural system is either conductive ($Ra_H < 868$), or has a Rayleigh–Roberts number so high that our approach cannot be applied ($Ra_H > 10^{10}$). The details of the modelling and parameters values are given in the text.

high to apply our approach (here chosen to be $Ra_H > 10^{10}$), or too low to allow for convection ($Ra_H < 868$). As a second step, we exclude all the cases where no melt is generated to focus only on the conditions for which melting is present (Fig. 11). In that regime, a surprising result is the absence of variations in the melting depths with increasing heating rate. This is actually caused by the simplified version of melting considered here (see Section 5.1.5). A more sophisticated modelling of melting should predict a widening of the melting depths with increasing heating rate. Furthermore, for heating rates as large as 10^{-4} W m^{-3}, one may expect the appearance of a local magma ocean. As a matter of fact, considering $R_{tp} =$ 1000 km and $H_{tp} = 10^{-4}$ W m^{-3}, a volume equivalent to the whole mantle should melt every 10 Myr. This may be difficult to reconcile with solid-state convection. Our results can therefore be seen as a preliminary step. A more sophisticated model of melting is thus required to obtain a precise assessment of melting in exoplanets.

Nevertheless, the present results already provide crucial and robust information that deserved to be discussed. For instance, the depth range where melting occurs exhibit two different trends with increasing planetary radius. For $R_{tp} < 1000$ km, the depth range becomes deeper with increasing planetary radius. In that case, the solidus temperature varies only slightly with depth due to the low acceleration of gravity. As a result, melting occurs from the base of the mantle to the base of the TBL. In other words, the maximum depth of melting is simply the mantle depth, while the minimum depth of melting varies as the thickness of the TBL (which is increasing with the planetary radius following Vilella & Kaminski 2017). One way to verify this observation is with the dimensionless average melting depth (Fig. 11d) that remains constantly high (>0.6) in that regime. For $R_{tp} > 1000$ km, the depth range becomes shallower with increasing planetary radius. This is because pressure variations are becoming significant inducing an increase of the melting temperature with the planetary radius. Melting therefore requires a higher effective heating rate, inducing a larger Ra_H so a thinner TBL. This trend is likely to remain valid for Ra_H larger than 10^{10} as long as the trend of the solidus profile with pressure is not significantly modified, which is unlikely to happen even for large exoplanets (Stixrude 2014).

6 CONCLUSION

We have developed a new analytical approach, partly based on an extended version of the MLT, able to estimate the distribution of the hottest temperatures for a purely volumetrically heated system. The final objective was to assess the melt generation in 1-D analytical models. We have therefore proposed a 1-D analytical approach that

accounts for the effects of melting, secular cooling and radioactive heating. To demonstrate its relevance, we applied this model to a generic planetary mantle and conducted a 3-D simulation reproducing these conditions. The comparison between the analytical results and the 3-D simulation are encouraging. In particular, the evolution of the maximum temperature and the depth range where melting occurs is well reproduced by our analytical approach. Note however that the volume average temperature is systematically underestimated by ∼70 K and that the total amount of melting is three times lower than in the 3-D simulation. Despite these disagreements, our analytical approach stands as a useful tool to study planetary evolution: (i) it is the only analytical approach able to constrain a part of the temperature distribution, that is able to model melt generation properly; (ii) compared to 2-D or 3-D simulations, 1-D analytical models are much faster so that a much larger parameter space can be explored and (iii) our analytical approach can be combined with a sophisticated modelling of melt generation in order to investigate the chemical evolution of planetary mantles. The latter point is crucial for our understanding of planetary evolution, while it seems out of reach for current 2-D and 3-D simulations. This study, however, considers a purely volumetrically heated fluid, which may not be appropriate to model accurately a planetary body. Additional work is therefore required to extend our analytical approach to a system appropriately depicting a planetary mantle or an icy shell.

ACKNOWLEDGEMENTS

We thank two anonymous reviewers for their thorough and constructive comments that helped us to improve this manuscript. We also thank G. Choblet for his editorial handling of the manuscript. This research was funded by JSPS KAKENHI Grant Number JP19F19023.

DATA AVAILABILITY

The data used for generating the figures are available for academic purposes (Vilella 2020). All required details to reproduce the analytical results are given in the text, while the numerical results have been detailed in a previous publication (Vilella *et al.* 2018). Note that the program used to calculate the analytical evolution reported in Fig. 9 is available for academic purposes (Vilella 2020). The numerical code used to obtain the numerical results is not publicly available but was thoroughly described in Tackley (2008).

REFERENCES

Abe, Y., 1993. Physical state of the very early Earth, *Lithos,* **30,** 223–235.

Andrault, D., Bolfan-Casanova, N., Lo Nigro, G., Bouhifd, M.A., Garbarino, G. & Mezouar, M., 2011. Solidus and liquidus profiles of chondritic mantle: implication for melting of the Earth across its history, *Earth planet. Sci. Lett.,* **304,** 251–259.

Ballmer, M.D., Lourenço, D.L., Hirose, K., Caracas, R. & Nomura, R., 2017. Reconciling magma-ocean crystallization models with the present-day structure of the Earth's mantle, *Geochem. Geophys. Geosyst.,* **18,** 2785–2806.

Breuer, D. & Spohn, T., 2003. Early plate tectonics versus single-plate tectonics on Mars: evidence from magnetic field history and crust evolution, *J. geophys. Res.,* **108**(E7).

Castaing, B. *et al.*, 1989. Scaling of hard thermal turbulence in Rayleigh-Bénard convection, *J. Fluid Mech.,* **204,** 1–30.

Choblet, G. & Sotin, C., 2000. 3D thermal convection with variable viscosity: can transient cooling be described by a quasi-static scaling law?, *Phys. Earth planet. Inter.,* **119,** 321–336.

Christensen, U.R. & Hofmann, A.W., 1994. Segregation of subducted oceanic crust in the convecting mantle, *J. geophys. Res.,* **99,** 19867–19884.

Davaille, A. & Jaupart, C., 1993. Transient high-Rayleigh-number thermal convection with large viscosity variation, *J. Fluid Mech.,* **253,** 141–166.

Driscoll, P. & Bercovici, D., 2014. On the thermal and magnetic histories of Earth and Venus: influences of melting, radioactivity, and conductivity, *Phys. Earth planet. Inter.,* **236,** 36–51.

Grasset, O. & Parmentier, E.M., 1998. Thermal convection in a volumetrically heated, infinite Prandtl number fluid with strongly temperature-dependent viscosity: implications for planetary thermal evolution, *J. geophys. Res.,* **103,** 18171–18181.

Grott, M., Breuer, D. & Laneuville, M., 2011. Thermo-chemical evolution and global contraction of mercury, *Earth planet. Sci. Lett.,* **307,** 135–146.

Hirschmann, M.M., 2000. Mantle solidus: experimental constraints and the effects of peridotite composition, *Geochem. Geophys. Geosyst.,* **1**(10).

Jeanloz, R. & Morris, S., 1987. Is the mantle geotherm subadiabatic?, *Geophys. Res. Lett.,* **14,** 335–338.

Jellinek, A.M. & Jackson, M.G., 2015. Connections between the bulk composition, geodynamics and habitability of Earth, *Nat. Geosci.,* **8,** 587–593.

Kamata, S., 2018. One-dimensional convective thermal evolution calculation using a modified mixing length theory: application to Saturnian icy satellites, *J. geophys. Res.,* **123,** 93–112.

Kaminski, E., Limare, A., Kenda, B. & Chaussidon, M., 2020. Early accretion of planetesimals unraveled by the thermal evolution of the parent bodies of magmatic iron meteorites, *Earth planet. Sci. Lett.,* **548**(A66).

Katz, R.F., Spiegelman, M. & Langmuir, C.H., 2003. A new parameterization of hydrous mantle melting, *Geochem. Geophys. Geosyst.,* **4**(9).

Kimura, J., Nakagawa, T. & Kurita, K., 2009. Size and compositional constraints of Ganymede's metallic core for driving an active dynamo, *Icarus,* **202,** 216–224.

Krishnamurti, R., 1968. Finite amplitude convection with changing mean temperature. Part 1. Theory, *J. Fluid Mech.,* **33,** 445–455.

Labrosse, S., 2002. Hotspots, mantle plumes and core heat loss, *Earth planet. Sci. Lett.,* **199,** 147–156.

Laneuville, M., Wieczorek, M.A., Breuer, D. & Tosi, N., 2013. Asymmetric thermal evolution of the moon, *J. geophys. Res.,* **118,** 1435–1452.

Limare, A. *et al.*, 2015. Microwave-heating laboratory experiments for planetary mantle convection, *J. Fluid Mech.,* **1565,** 14–18.

Limare, A., Kenda, B., Kaminski, E., Surducan, E., Surducan, V. & Neamtu, C., 2021. Transient convection experiments in internally-heated systems, *MethodsX,* **8**.

Lourenço, D.L., Rozel, A.B., Gerya, T. & Tackley, P.J., 2018. Efficient cooling of rocky planets by intrusive magmatism, *Nat. Geosci.,* **11,** 322–327.

Monteux, J., Andrault, D. & Samuel, H., 2016. On the cooling of a deep terrestrial magma ocean, *Earth planet. Sci. Lett.,* **448,** 140–149.

Morschhauser, A., Grott, M. & Breuer, D., 2011. Crustal recycling, mantle dehydration, and the thermal evolution of Mars, *Icarus,* **212,** 541–558.

Parmentier, E.M. & Sotin, C., 2000. Three-dimensional numerical experiments on thermal convection in a very viscous fluid: Implications for the dynamics of a thermal boundary layer at high Rayleigh number, *Phys. Fluids,* **12,** 609–617.

Roberts, P.H., 1967. Convection in horizontal layers with internal heat generation. Theory, *J. Fluid Mech.,* **30,** 33–49.

Samuel, H. & Farnetani, C.G., 2003. Thermochemical convection and helium concentrations in mantle plumes, *Earth planet. Sci. Lett.,* **207,** 39–56.

Sasaki, S. & Nakazawa, K., 1986. Metal-silicate fractionation in the growing Earth: Energy source for the terrestrial magma ocean, *J. geophys. Res.,* **91,** 9231–9238.

Sharpe, H. & Peltier, W.R., 1978. Parameterized mantle convection and the Earth's thermal history, *Geophys. Res. Lett.,* **5,** 737–740.

Silveston, P.L., 1958. Wärmedurchgang in waagerechten Flüssigkeitsschichten, *Forschung auf dem Gebiet des Ingenieurwesens A,* **24,** 59–69.

Sinha, G. & Butler, S.L., 2007. On the origin and significance of subadiabatic temperature gradients in the mantle, *J. geophys. Res.,* **112**(B10).

Sotin, C. & Labrosse, S., 1999. Three-dimensional thermal convection in an iso-viscous, infinite Prandtl number fluid heated from within and from below: applications to the transfer of heat through planetary mantles, *Phys. Earth planet. Inter.,* **112,** 171–190.

Spiegel, E.A., 1963. A generalization of the mixing-length theory of turbulent convection, *Astrophys. J.,* **138,** 216–225.

Steinke, T., Hu, H., Höning, D., van der Wal, W. & Vermeersen, B., 2020. Tidally induced lateral variations of Io's interior, *Icarus,* **335**.

Stevenson, D.J., Spohn, T. & Schubert, G., 1983. Magnetism and thermal evolution of the terrestrial planets, *Icarus,* **54,** 466–489.

Stixrude, L., 2014. Melting in super-earths, *Phil. Trans. R. Soc., A,* **372**(2014).

Tachinami, C., Senshu, H. & Ida, S., 2011. Thermal evolution and lifetime of intrinsic magnetic fields of Super-Earths in habitable zones, *Astrophys. J.,* **726**(2).

Tackley, P.J., 2008. Modelling compressible mantle convection with large viscosity contrasts in a three-dimensional spherical shell using the yin-yang grid, *Phys. Earth planet. Inter.,* **171,** 7–18.

Valencia, D., O'Connell, R.J. & Sasselov, D., 2006. Internal structure of massive terrestrial planets, *Icarus,* **181,** 545–554.

Vilella, K., 2021. Application of the mixing length theory to assess the generation of melt in internally heated systems, *Mendeley Data,* Version 3, doi: 10.17632/vyhhgsz336.3.

Vilella, K. & Kaminski, E., 2017. Fully determined scaling laws for volumetrically heated convective systems, a tool for assessing habitability of exoplanets, *Phys. Earth planet. Inter.,* **266,** 18–28.

Vilella, K., Limare, A., Jaupart, C., Farnetani, C., Fourel, L. & Kaminski, E., 2018. Fundamentals of laminar free convection in internally heated fluids at values of the Rayleigh-Roberts number up to 10^9, *J. Fluid Mech.,* **846,** 966–998.

Vilella, K., Choblet, G., Tsao, W.E. & Deschamps, F., 2020. Tidally heated convection and the occurrence of melting in icy satellites: application to Europa, *J. geophys. Res.,* **125**(3).

Vitense, E., 1953. Die Wasserstoffkonvektionszone der Sonne, *Zeitschrift für Astrophysik,* **32,** 135–164.

Wagner, F.W., Plesa, A.C. & Rozel, A.B., 2019. Calibrating mixing-length theory for thermal convection in rocky planets, *J. geophys. Int.,* **217,** 75–89.

Weinstein, S.A. & Olson, P., 1990. Planforms in thermal convection with internal heat sources at large Rayleigh and Prandtl numbers, *Geophys. Res. Lett.,* **3,** 239–242.

Xie, S. & Tackley, P.J., 2004. Evolution of helium and argon isotopes in a convecting mantle, *Phys. Earth planet. Inter.,* **146,** 417–439.

Zhang, J. & Herzberg, C., 1994. Melting experiments on anhydrous peridotite KLB-1 from 5.0 to 22.5 GPa, *J. geophys. Res.,* **99,** 17729–17742.

SUPPORTING INFORMATION

Supplementary data are available at *GJI* online.

Figure S1. Dimensionless surface heat flux calculated from the hot temperature profile as a function of the Rayleigh–Roberts number (Ra_H). The results are from the 3-D numerical simulations conducted in Vilella et al. (2018). We also plot the constant dimensionless value 1.65 that is used in this work as a reference value.

Figure S2. Solidus profile used in our analytical approach. This profile is built by combining and interpolating experimental works on terrestrial peridodites (Hirschmann, 2000; Zhang & Herzberg, 1994; Andrault et al., 2011).

Figure S3. Horizontally averaged (left column) and hot (central column) temperature profiles as well as X_M the proportion of material whose temperature is larger than the solidus temperature (right column) for (a) $Ra_H = 10^6$ and (b) $Ra_H = 10^9$. Blue curves are obtained from 3-D numerical simulations, while red curves are calculated with our analytical framework. In the right column, the blue shaded area reproduces the temporal fluctuations exhibited by the 3-D numerical results.

Figure S4. Plot of the function f^* (black curves) used in our analytical model and gradient of the temperature profile obtained by our analytical model with $Ra_H = 10^9$ (red curves) for the average temperature profile. Note that the x-axis has a logarithmic scale for visualization purposes.

Figure S5. Evolution of the (a) effective heating rate (H_{eff}), (b) the power associated with melt generation (H_{melt}), (c) the radioactive heating rate (H_{rad}), and (d) the secular cooling contribution (H_{sec}) estimated using our analytical approach for the generic mantle described in Section 4.1. The red, purple and blue curves are obtained favouring a maximum amount of melting of 4.5, 2.0 and 0.5 per cent, respectively. This figure is complementary to Fig. 10.

Figure S6. Evolution of the (a) maximum temperature, (b) the volume average temperature, (c) the depths where melting occurs and (d) the melting rate for the generic mantle described in Section 4.1. The different curves are obtained using a different value of Δt_{ev} comprises between 1 Myr and 1 kyr. Except for the melting rate, the curves are superimposed. The melting rate is impacted by Δt_{ev}, because it influences how the maximum proportion of melting decreases with time. This is for example responsible for the stepwise variations visible for $\Delta t_{\mathrm{ev}} = 10$ and 1 kyr. Overall, the difference in term of total volume of melt generated is less than 0.02 per cent between cases with $\Delta t_{\mathrm{ev}} = 100$, 10 and 1 kyr, while this difference rises to 0.5 per cent when considering cases with $\Delta t_{\mathrm{ev}} = 1$ Myr and 100 kyr. Values of Δt_{ev} lower than 100 kyr are therefore required to ensure a correct depiction of the evolution.

Please note: Oxford University Press is not responsible for the content or functionality of any supporting materials supplied by the authors. Any queries (other than missing material) should be directed to the corresponding author for the paper.

APPENDIX: SOLVING THE GOVERNING EQUATION

The resolution of eq. (11) is achieved using a finite difference approach. More specifically, the discretization of eq.(11) implies,

$$\frac{T^*_{i+1} - T^*_i}{\mathrm{d}z} - \frac{Ra_H l_i^{*4}}{18}\left(\frac{T^*_{i+1} - T^*_i}{\mathrm{d}z} - f^*(z^*_i)\right)^2 + z^*_i = 0, \qquad \text{(A1)}$$

where T^*_i and l^*_i are the temperature and mixing length at height z^*_i, and T^*_{i+1} the temperature at height $z^*_{i+1} = z^*_i + \mathrm{d}z$, with $\mathrm{d}z$ a small increment. This equation allows to calculate T^*_i from T^*_{i+1} by solving a second order polynomial equation. A difficulty, however, is to choose the correct solution from the two solutions of the polynomial equation. To do so, we select the solution given the best continuity in term of temperature gradient. As a result, the increment $\mathrm{d}z$ has to be very small in order to ensure that the correct solution is chosen. For reference, we typically use 50 000 vertical points to safely prevent any possible problems. Note that the same method can be followed to calculate the hot temperature profile from eq. (15).